Australian Government

Department of Defence
Science and Technology

Signal Separation Of Helicopter Radar Returns Using Wavelet-Based Sparse Signal Optimisation

Si Tran Nguyen Nguyen[1], *Sandun Kodituwakku*[2], *Rocco Melino*[2] *and Hai-Tan Tran*[2]

[1] **The University of Adelaide**
[2] **National Security and ISR Division**
Defence Science and Technology Group

DST-Group–RR–0436

ABSTRACT

A novel wavelet-based sparse signal representation technique is used to separate the main and tail rotor blade components of a helicopter from the composite radar returns. The received signal consists of returns from the rotating main and tail rotor blades, the helicopter body, possible land or sea clutter, and other residual components, which may all overlap in time and frequency; and therefore conventional time and frequency separation techniques cannot be applied. A sparse signal representation technique is now proposed for this problem with the tunable Q wavelet transform used as the dictionary. The proposed algorithm is demonstrated using both simulated and real radar data (X and Ku-band), and is capable of extracting the components of interest successfully.

RELEASE LIMITATION

Approved for public release

Signal Separation Of Helicopter Radar Returns Using Wavelet-Based Sparse Signal Optimisation

Executive Summary

The radar return from a helicopter target in flight is a complex multi-component signal comprising of returns from the main body, the main and tail rotor hubs and blades. Temporal and Doppler characteristics of these components are quite distinguishable providing a potential basis for automatic target recognition and classification. For example, the blade returns are highly non-stationary and have a broad Doppler spectrum in periodic short time intervals. On the other hand, the body return is relatively stationary with a narrow Doppler line. Separating composite radar return into individual components provides useful information for number of Defence applications. In this report, we propose robust algorithms for separating main rotor blade component, as well as that of the tail rotor blade, from the other components using state-of-the-art wavelet transforms and sparse signal representation techniques.

Wavelet transforms have been used extensively to transform a signal into the time-scale domain, simultaneously representing time and frequency information. Among the recently developed classes of discrete wavelets, the tunable Q wavelet transform (TQWT) offers great flexibility to represent the signal components of interest, and can also be efficiently implemented. In this work, the TQWT is used to represent the main and tail rotor blade returns, which can then be extracted by sparse signal optimisation. A variation of basis pursuit denoising (BPD), an l_1 norm based sparse optimisation technique, is used to compute the TQWT coefficients. Two algorithms are presented in the report to separately extract main rotor blade returns and tail rotor blade returns from the composite signal.

The algorithms are demonstrated on both simulated and real helicopter data. The experimental data at X-band (9.5 GHz) and Ku-band (16.8 GHz) were collected by the DST Wandana II radar of a Squirrel AS350BA helicopter at various aspect angles. The algorithms are shown to be capable of extracting the main rotor blade signal as well as the tail rotor blade signal almost completely, leaving only the hub and body components in the residual signal. Also, no artifacts in the extracted signals were observed despite the presence of the dominant body component and noise. Comparisons of the original and extracted signals in time and frequency domains show an excellent match.

The proposed method is also tested in a typical sea clutter environment. Simulated sea clutter was added to X-band helicopter data at different signal-to-clutter ratios (SCR), and the performance of the methods is verified. Even at a total SCR of -11.7 dB (the main blades SCR is -25 dB), the main rotor blade returns were successfully extracted from other signal components and clutter.

Future work is required to test the performance of the proposed methods when applied to a highly maneuvering helicopter. Also, the performance of the algorithms at other operating frequencies such as L or S-band is still to be evaluated using real data. More work on automatic tuning of the TQWT filter is also warranted. The proposed methods are highly flexible, and can be adapted to analyse radar returns from other rotating blade structures such as wind turbines.

THIS PAGE IS INTENTIONALLY BLANK

Authors
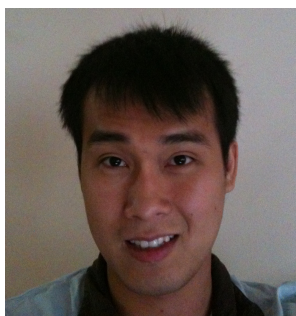
Dr Si Tran Nguyen
The University of Adelaide

Si Tran Nguyen graduated from the University of Adelaide in 2007 with first class honours and worked for Codan Limited, South Australia as a microwave graduate engineer in the following year. In 2014, he obtained his PhD from the school of Electrical and Electronic Engineering, the University of Adelaide with the thesis entitled: Design of bi-orthogonal rational Discrete Wavelet Transform and the associated applications with Deans Commendation for Doctoral Thesis Excellence. From 2012, he has been with the University of Adelaide Radar Research Centre and working on various projects including wavelet based clutter mitigation for weather radar, Synthetic Aperture Radar software development, and Helicopter radar signal separation with the Bureau of Meteorology and DST Group, respectively. His research interests include rational rate Filter Banks, Rational Dilation Wavelet Transforms, sparse signal representation and applications, and radar signal processing.

Dr Sandun Kodituwakku
National Security and ISR Division

Sandun Kodituwakku received a Bachelor of Engineering (Electrical and Electronic) with first class honours from the University of Adelaide in 2006, and a PhD in biomedical signal processing from the Australian National University in 2012. He works as a radar signal processing researcher at DST Group since 2011. His research interests include radar detection, adaptive signal processing, automatic target recognition, radar imaging, and various topics in radar signal processing.

Mr Rocco Melino
National Security and ISR Division

Rocco Melino received a Bachelor Degree in Electronic Engineering from the University of South Australia in 1999 and has a Masters Degree in Signal and Information Processing from the University of Adelaide. He has been working for the National Security and ISR Division of DST Group, since 1999, in the branch of microwave radar. His research interests include radar automatic target recognition, radar modelling and signal processing.

Dr Hai-Tan Tran
National Security and ISR Division

Hai-Tan Tran graduated from the University of Sydney in 1990 and obtained his PhD degree from the Australian National University in Canberra in 1993, in the field of nonlinear guided-wave optics. He spent the next three years as a postdoctoral research fellow in the Mathematics Department of the Australian Defence Force Academy, also in Canberra, working on the theory and simulation of spatial optical solitons and light-induced optical switching in nonlinear dielectric media, before joining the National Security and ISR Division of DST Group, Edinburgh, in 1996. His current research interests include high-resolution radar imaging, automatic target recognition, radar electronic protection, and various topics in signal processing.

Contents

List of Figures

Glossary

BP	Basis Pursuit
BPD	Basis Pursuit Denoising
CPI	Coherent Processing Interval
DC	Direct Current
DFT	Discrete Fourier Transform
DST Group	Defence Science and Technology Group
FIR	Finite Impulse Response
GIT	Georgia Institute of Technology
GPARM	Generic Phased Array Radar Model
ISAR	Inverse Synthetic Aperture Radar
JEM	Jet Engine Modulation
OMP	Orthogonal Matching Pursuit
PRF	Pulse Repetition Frequency
RADWT	Rational Dilation Wavelet Transform
RPM	Revolutions per Minute
SAR	Synthetic Aperture Radar
SCR	Signal to Clutter Ratio
SALSA	Split Augmented Lagrangian Shrinkage Algorithm
STFT	Short Time Fourier Transform
TQWT	Tunable Q Wavelet Transform
WT	Wavelet Transform

Notation

θ	The weighting parameter of the BPD
λ	The compensation vector of the TQWT
$\boldsymbol{\Phi}$	TQWT forward transform matrix
$\boldsymbol{\Phi}^{-1}$	TQWT inverse transform matrix
l_1	l_1 norm
l_2	l_2 norm
J	Level of decomposition of the filter bank (wavelet transform)
Q	Q factor of the constant Q wavelet transform
r	Redundancy factor of the TQWT

THIS PAGE IS INTENTIONALLY BLANK

1   Introduction

Radar returns from a helicopter target in flight is a complex signal composed of multiple signal components due to rotating and vibrating parts on the helicopter body including the main and tail rotor blades, rotor hubs, body of the helicopter, and interference sources such as sea clutter. Some components are relatively stationary such as returns from the helicopter body, whereas others are highly non-stationary such as the returns from the rotating blades, where the high and different angular velocities of the main and tail rotor blades induce wide Doppler frequency spreads in the return signal, and are observable as short periodic 'blade flashes' in the time domain. These blade flashes belong to the class of micro-Doppler signals [1, 2, 3], which cannot be conveniently processed by standard range-Doppler processing techniques.

In this report, we exploit sparse signal representation techniques for the problem of signal separation for helicopter radar returns. The sparsity characteristics of such different signal components in the wavelet or time-scale domain can be used to differentiate and extract the signal components of interest. The extracted components can then be used for target imaging and classification, which is currently outside the scope of this work.

In recent years, signal processing techniques based on joint time-frequency distributions have been widely used to analyse radar micro-Doppler signatures, such as in the pioneering work by Chen et al. [1, 4, 2]. These authors developed mathematical models for micro-Doppler motion of vibrating, rotating, tumbling, and coning point scatterers and effects of radar platform vibration on micro-Doppler modulation. They used linear time-frequency transforms such as short-time Fourier transform (STFT), Cohen's class of bilinear transforms such as Wigner-Ville and Choi-Williams, as well as adaptive time-frequency transforms in the context of micro-Doppler signature analysis. Order statistics combined with time-frequency representation is used by Stankovic et al. [5, 6] to separate micro-Doppler returns from the rigid body returns. In this work, a linear combination of order statistics called *'L-statistics'* is used to differentiate non-stationary micro-Doppler signals from the relatively stationary rigid body return.

Time-frequency analysis has long been a useful tool for many applications across different fields, such as blind separation of speech signals [7], machinery fault diagnosis [8] and radar imaging and signal analysis [9]. The aim is to obtain a representation domain in which the signal components of interest can be efficiently represented. For example, an infinitely long and periodic signal can be represented by a number of sinusoids of varying coefficients in the Fourier domain – the classical Fourier series. For signals with finite time support, the conventional Fourier transform is inadequate, and other time-frequency analysis tools such as the short-time Fourier transform (STFT), Gabor transform [10] and the wavelet transform [11] have been devised for their representation.

A time-frequency filter and Viterbi algorithm based method was proposed by Li et al. [12] for separation of micro-Doppler signals. The Viterbi algorithm was applied in the time-frequency domain to estimate instantaneous frequencies of signal components, and then a time-frequency filter was designed to filter and synthesise the micro-Doppler signals of interest. For helicopter radar returns the fast rotating blades give rise to broad instantaneous Doppler frequency terms in the signal; a single instantaneous frequency cannot be defined.

In addition to the Fourier based analysis, a number of different basis functions for time-

frequency analysis have been proposed for micro-Doppler signal representation. In [13] the radar returns are decomposed into stationary and non-stationary components using the Fourier-Bessel transform in conjunction with the fractional Fourier transform, and time-frequency analysis was used to estimate the target's motion parameters after the extraction of micro-Doppler features. An adaptive chirplet representation was used in [14], and the signals from the body and the rotating parts were then separated in the chirplet parameter space. A set of basis functions with sinusoidal phase was proposed in [15], given the fact that micro-Doppler signals from rotating point scatterers are sinusoidal in the time-frequency domain.

Statistical signal separation techniques have been proposed for micro-Doppler signal separation. Singular spectrum analysis is a non-parametric spectral estimation technique based on the singular value decomposition, and has been applied to extract micro-Doppler effects in ISAR imaging [16] and SAR imaging in clutter [17]. Going beyond the second order statistics, techniques for micro-Doppler feature extraction based on spatio-temporal independent component analysis have been proposed in [18]. Empirical mode decomposition which decomposes radar returns into intrinsic mode functions was applied to extract micro-Doppler signals and generate focused ISAR images [19, 20]. In [21], empirical mode decomposition followed by the Hilbert spectrum was applied to analyse micro-Doppler signatures, and superior results to Cohens class of time-frequency distributions have been obtained.

More recently, compressive sensing based signal separation algorithms were proposed to decompose multi-component signals [22, 23, 24, 25, 26, 27]. In [22], for the separation of micro-Doppler and main body signatures, compressive sensing signal reconstruction was used to recover stationary narrowband signals in the presence of strong non-stationary signals. Overlapping points in the time-frequency domain are cast as missing samples, and l_1 minimisation was used to reconstruct the signal using sparsity of the stationary components in the frequency domain. A similar compressive sensing based technique for linear FM signals, which are associated with accelerating targets, is presented in [23], where the local polynomial Fourier transform is applied to demodulate chirp signals before signal reconstruction.

A number of image processing methods have also been applied to the problem of micro-Doppler signal separation. The Hough transform which has been widely used for line segment detection, and the extended Hough transform have been used for micro-Doppler signal analysis [28, 29, 30]. In these methods, the detection of the straight lines and the sinusoids in the time-frequency image are assumed to correspond to the non-rotating parts and the rotating parts, respectively. But returns from helicopter rotor blades also exhibit straight lines in the time-frequency plane with a 90 degree slope, thus the above assumption does not hold for micro-Doppler of helicopter returns. The Radon transform, which can transform a sinusoidal phase modulated signal (a rotating point scatterer in time-frequency plane) into a single point, was also applied in micro-Doppler analysis [5]. These types of pattern recognition algorithms work effectively only when the returns from the rotating parts are significant compared to the body return, which is often not the case.

Most related to the current report is a simple 4-level decomposition with db1 wavelet based method proposed by Thayaparan et al. [31] for analysing radar micro-Doppler signatures from experimental helicopter and human data. Their decomposition method is not really designed to fully represent the 'deep level' information from micro-Doppler radar signatures. Other methods for micro-Doppler signal analysis and separation include complex local mean decomposition [32] and a delay-line technique [33], which was used for clutter cancellation.

The general limitations of these known techniques are as follows.

- Most methods remove micro-Doppler components to generate a well focused image of the rigid body of a target, rather than extracting useful information from the micro-Doppler signals for further processing.

- Most of the above methods have only been tested for simple cases of simulated and real data, assuming a rotating point scatterer model which generates a sinusoidal phase modulated signal. For example, a sinusoidal phase modulated signal (non-stationary micro-Doppler signal) with multiple sinusoids (stationary rigid body signal), or an aircraft return with JEM lines; to our knowledge, the complexity of returns from a blade structure as in the case of helicopter returns has not been adequately studied.

- Most importantly, the existing methods separate the rigid body component from micro-Doppler components, but do not decompose micro-Doppler returns into individual sub-components. For example, current methods cannot be used to separate radar returns of the tail rotor and the main rotor of a helicopter.

1.1 Micro-Doppler signal representation for a helicopter

Consider the received signal from a helicopter target in flight as a complex time series $\boldsymbol{x}[n]$, with components

$$\boldsymbol{x}[n] = \boldsymbol{x}_{MB}[n] + \boldsymbol{x}_{TB}[n] + \boldsymbol{x}_B[n] + \boldsymbol{r}[n], \tag{1}$$

where n denotes the slow-time sample index, $\boldsymbol{x}_{MB}, \boldsymbol{x}_{TB}$ represent the returns from main and tail rotor blades respectively, $\boldsymbol{x}_B$ is the return from the helicopter body, and $\boldsymbol{r}[n]$ represents other interference components such as clutter and noise. A typical spectrogram of real helicopter data is presented in Figure 1, showing the components of $\boldsymbol{x}[n]$.

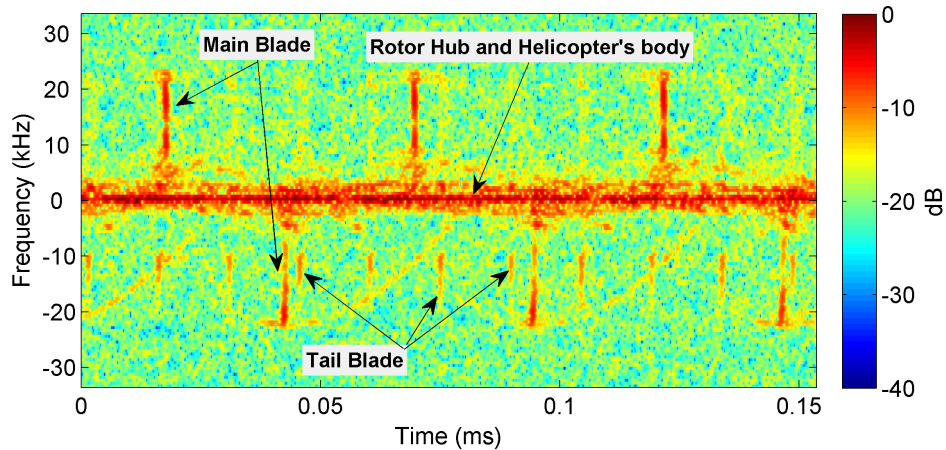*Figure 1: Spectrogram of the original Ku-band radar signal (HH polarisation) showing the different components: main blades, tail blades, and low Doppler frequency components associated with the rotor hub and helicopter body.*

It should be noted in Figure 1 that the Doppler characteristics of both the main and tail blades are quite similar, however the main blades usually exhibit broader Doppler bandwidths and

a stronger magnitude (for HH return) due to its physical structure (longer blade length), and the aspect angle viewed by the radar. At broad beam aspects, the main blades' Doppler bandwidths are generally broader than those of the tail blades. On the other hand, closer to the 'top-down' or 'bottom-up' aspects, the Doppler bandwidths of the tail rotor may be broader.

One of the aims of this work is to extract the components from main rotor blades out of the composite signal, followed by a similar extraction for the tail blades using a representation domain in which the signal components of interest can be efficiently represented. Although the components in the composite signal overlap in both time and frequency, they exhibit different temporal and Doppler characteristics. The main and the tail rotor blades can be observed to have broad and different Doppler and temporal characteristics (highly non-stationary) compared to the hub and body components (relatively stationary).

To achieve micro-Doppler signal separation for this application, the use of wavelet transforms to represent the main and tail blade signals in the time-scale domain is applied and then these components are extracted using sparse signal optimisation techniques.

Generally, a wavelet transform maps a signal in the time domain into the time-scale domain which gives the frequency information of the original signal and the times at which these frequency components occur; time and frequency (or scale) are two fundamental properties to describe a signal. To describe complex and diverse signals in the real world, there is also an important third property: resonance [34]. The resonance of an isolated pulse is quantified by its 'Q-factor', defined as the ratio of its centre frequency f_c to its bandwidth BW, i.e., $Q = f_c/BW$, and is directly proportional to the number of cycles (or oscillations) in the pulse.

If we only consider the frequency aspect of the wavelet transform, it can be viewed as a sub-band decomposition, such that each frequency sub-band has the same Q-factor, being approximately 1.5 for the conventional dyadic discrete wavelet transform [11, 35]. Recently, with the advances in computational power and the need for representing various classes of signals, research in developing new families of discrete wavelets, termed as Rational-Dilation Wavelet Transforms (RADWT), as discussed in [36, 37, 38, 39, 40, 41], allows more flexibility in specifying the Q factor. The driving motivation is to design the Q factor that best suits the signal class of interest.

The tunable Q wavelet transform (TQWT) first discussed by Selesnick in [38] is among the newly developed RADWTs and is chosen for our application since it is simple to implement and offers great flexibility through tuning of the Q-factor and other parameters (the transform parameters), which are critical for the sparse representation of the signals of different frequency and temporal characteristics. Other work to apply the TQWT to a radar problem was on sea clutter mitigation [42], in which resonance-based signal separation was exploited to separate the sea clutter and the target components using a sparse optimisation routine with the dictionary being constructed based on TQWTs.

The algorithms presented in this report based on wavelet transforms and sparse signal representation will address the above shortcomings, and can be used to extract different levels of target information, such as the returns from main rotor blades, and tail rotor blades, as well as being robust to sea clutter interference. These signal separation algorithms are presented in Section 2. The results for simulated and real experimental data are presented in Sections 3

and [4], respectively. In Section [5], the performance of the algorithm in a clutter contaminated environment is analysed. Parameter selection, computational cost of the algorithms, and algorithm performance for lower carrier frequencies are discussed in Section [6]. Finally, Section [7] presents some concluding remarks.

2   Analysis Methods

The algorithm proposed in this report is based on the TQWT and sparse signal optimisation techniques for the separation of the main and tail rotor blades from the body return, in both clutter free and clutter contaminated environments. The success of the techniques is based on the use of TQWT to efficiently represent the signal components of different Doppler and temporal characteristics. Once the suitable TQWTs are chosen for different components in the composite signal, they are separated by solving an l_1-optimisation problem with l_2 least square error, known as the basis pursuit denoising (BPD) problem.

The TQWTs offer a great flexibility in specifying the transform parameters and are efficient to implement numerically; it is indeed a suitable tool to analyse the signal components of interest, $\boldsymbol{x}_{MB}$ and $\boldsymbol{x}_{TB}$ in [(1)]. Sparsity of the representation is then optimised to effectively separate out the components. This section describes the TQWT in some detail.

2.1   Tunable Q Wavelet Transform

The three adjustable parameters of the TQWT are: the Q-factor, the redundancy parameter r, and the number of subbands J.

The redundancy parameter r characterises the degree of 'over-completeness' of the wavelet transform. Consider a discrete signal $\boldsymbol{x}$ represented by an $N \times 1$ column vector. A non-redundant wavelet transform has $r = 1$, and the transform matrix Φ and its inverse Ψ are $N \times N$ matrices. In such cases, a given signal $\boldsymbol{x}$ can be uniquely represented in the wavelet domain, as

$$\boldsymbol{x} = \Psi \boldsymbol{w}, \tag{2}$$

where $\boldsymbol{w}$ is a coefficient vector of length N. This denotes a linear equation system of N variables and N equations with a unique solution $\boldsymbol{w}$ for the invertible matrix Ψ.

When Ψ is a $N \times M$ matrix, with $M > N$, there are more wavelet functions in Ψ representing the signal than the length of the signal; the redundancy factor is greater than unity, $r = M/N > 1$. For a given signal $\boldsymbol{x}$, a solution for [(2)] is not unique, which can give a flexibility to optimise for the representation sparsity since M is the number of 'atoms' in the 'dictionary' Ψ. The transform matrix Φ of size $M \times N$ is composed of the analysis wavelet functions, and may be symbolically written as

$$\Phi = \left[\psi_{1,0}; \ldots; \psi_{1,k_0-1}; \; \psi_{2,0}; \ldots; \psi_{2,k_1-1}; \; \ldots; \psi_{J,0}; \ldots; \psi_{J,k_{J-1}-1}; \; \phi_0; \ldots; \phi_{L-1} \right], \tag{3}$$

where $\psi_{j,k}$ are row vectors representing the mother wavelet functions; a semicolon designates 'next row'; subscripts j and k here represent the scale (frequency) and time translation indices; and the ϕ_l functions, with $l = 0, \ldots, L-1$, are the 'father wavelet' functions. There are $J+1$
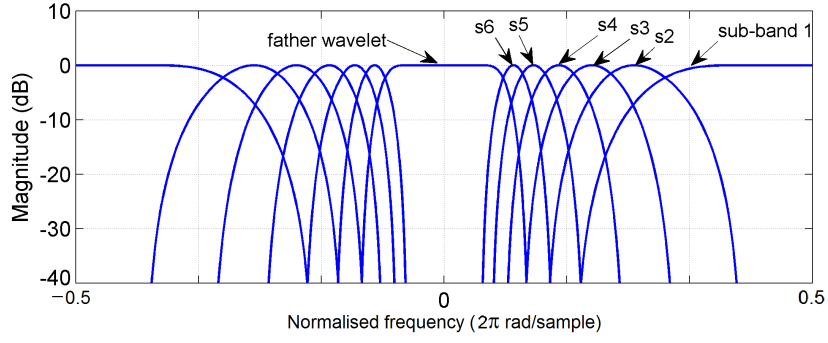
(a) The sub-band decomposition (sub-bands 1 to 6)
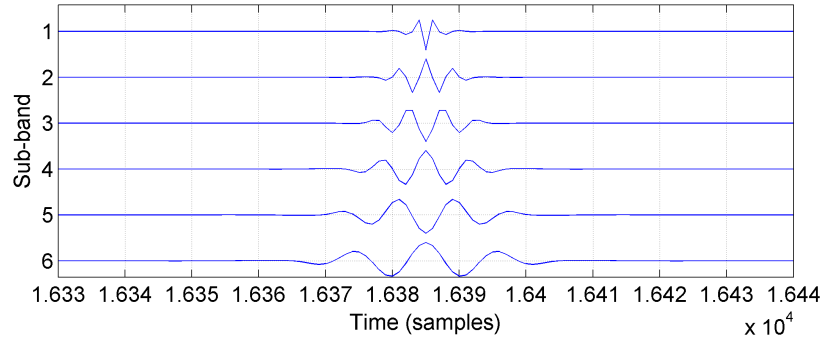
(b) Mother wavelet functions (sub-bands 1 to 6)
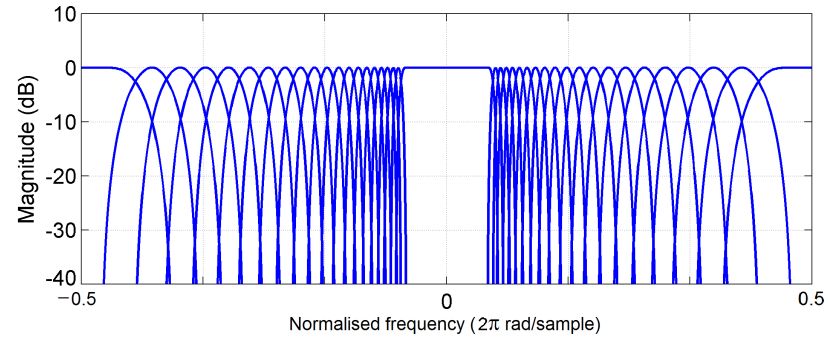
(c) Sub-band decomposition (sub-bands 1 to 20)
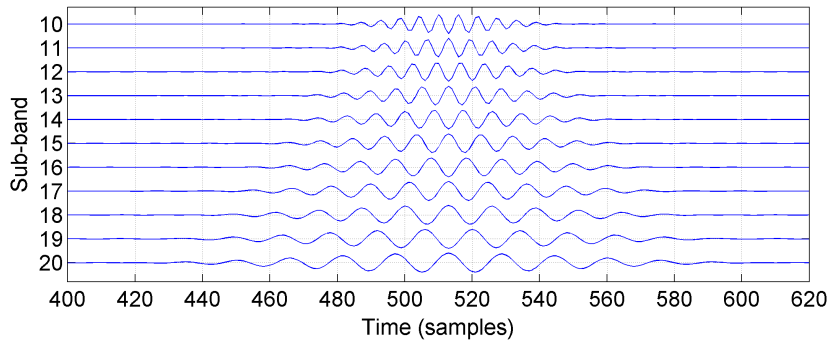
(d) Mother wavelet functions (sub-bands 10 to 20)

Figure 2: Examples of TQWT designs: (a) and (b) for $Q = 2, J = 6$ and $r = 2$; (c) and (d) for $Q = 6, J = 20$ and $r = 3$.

scales, or sub-bands, including the lowest frequency band spanned by the father wavelets. The scale index j ranges over $j = 1, 2, \ldots, J$, while the ranges for k depends on a sub-band.

For example, the mother wavelet functions $\psi_{1,k}$ with $k = 0, \ldots, k_0 - 1$ represents k_0 time-translated versions of a mother wavelet function at the first (coarsest) scale, and these mother wavelet functions will all have the same highest band-pass frequency response. The next mother wavelet function k_1 with scale index $j = 2$ occupies the next highest band-pass frequency region, and so on. The bandwidth of each of these frequency sub-bands are determined by the single predefined Q factor described earlier. We also have

$$k_0 + k_1 + \cdots + k_{J-1} + L = M,$$

i.e., the combined number of all mother and father wavelet functions, and all their time translations, is equal to M.

Figure 2(a) illustrates the sub-band decomposition associated with a TQWT with $Q = 2, J = 6, r = 2$, showing the 6 mother wavelet functions and 1 father wavelet function. The wavelet transform can be regarded as a sub-band decomposition operation in the frequency domain, where each of the mother and father wavelet functions and the corresponding time translations occupy one frequency sub-band. Figure 2(b) shows the time-domain mother wavelet functions corresponding to sub-bands 1 to 6. Here, $\psi_{1,j}$ represents the mother wavelet function corresponding to sub-band 1. The time index j represents the time translations of the mother wavelet, all of which have the same high frequency response as shown in Figure 2(a).

Similarly, the functions $\psi_{2,j}, \cdots, \psi_{6,j}$ are associated with the lower sub-bands, from 2 to 6. The father wavelet functions ϕ_l is associated with the low-pass spectrum as indicated in Figure 2(a). Altogether they span the frequency spectrum of the signal.

Figures 2(c) and 2(d) illustrate another TQWT example with a higher Q factor: $Q = 6$, while $J = 20$, $r = 3$. The higher Q value results in a denser sub-band decomposition and more oscillatory characteristics of the wavelet functions in the time-domain shown in Figure 2(d).

In summary, the following comments can be made about the TQWT:

1. The Q factor characterises the resonance level of all wavelet functions;

2. The number of sub-bands, J, is designed such that the set of all mother wavelets and the father wavelet completely span the frequency spectrum of the signal of interest. The lowest band around zero frequency is occupied by the father wavelet;

3. The redundancy parameter r, describes the degree of over-completeness of the wavelets;

4. When $M > N$, $\boldsymbol{\Phi}$ is generally not an invertible matrix, $\boldsymbol{\Psi}$ is a pseudo-inverse (or left-inverse) of $\boldsymbol{\Phi}$; these matrices are computed only implicitly as part of the filter design for the TQWT.

2.1.1   Implementation of the TQWT

The implementation of the TQWT is fully described in the paper by Selesnick [38]. One of the key advantages of the TQWT is the matrices $\boldsymbol{\Phi}$ and $\boldsymbol{\Psi}$ do not need to be constructed
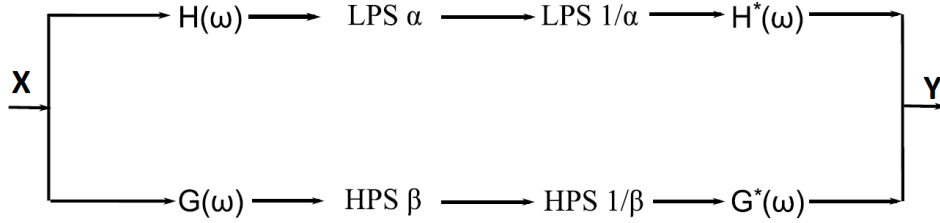
Figure 3: Perfect reconstruction filter bank structure for TQWT design, including the analysis low-pass and high-pass filters $H(\omega)$, $G(\omega)$ and associated synthesis filters $H^*(\omega), G^*(\omega)$. LPS and HPS are low and high pass rescaling operations, in frequency domain, with $\beta = 2/(Q+1); \alpha = 1 - \beta/r$. Perfect reconstruction means $\boldsymbol{X} = \boldsymbol{Y}$.

explicitly a priori, giving a significant saving in computing memory. Instead, the forward and inverse transforms can be implemented using an iterative strategy, where the input signal $\boldsymbol{x}$, its respective Fourier transform $\boldsymbol{X}(\boldsymbol{\omega})$, the transform parameters Q, r, J, and the corresponding wavelet coefficients $\boldsymbol{w}$ are computed iteratively, and vice versa.

For convenience of reference, the key points from the work in [38] on TQWT design and implementation are summarised below (using Figure 3 and 4, to aide the discussion):

1. Similar to other discrete wavelet transform designs, TQWT is designed based on a perfect reconstruction multi-rate filter bank structure, illustrated in Figure 3, for input $\boldsymbol{X}$ being equal to output $\boldsymbol{Y}$. Therefore, for a predefined Q-factor and r parameters, the transform is implemented using a perfect reconstruction over-sampled filter bank with real-valued sampling factors; $H(\omega)$, $G(\omega)$ are the analysis low-pass and high-pass filters, $H^*(\omega), G^*(\omega)$ are the synthesis low-pass and high-pass filters, respectively, where the responses $|H(\omega)| = |H^*(\omega)|$ and $|G(\omega)| = |G^*(\omega)|$. This effectively means that the frequency spectrum of the synthesis father and mother wavelets (those that construct the inverse transform Ψ) are identical to the analysis counterparts which constitute the forward transform matrix Φ.

   It should be noted that this filter bank structure is implemented in the frequency domain, i.e., the input and output signals, $\boldsymbol{X}$ and $\boldsymbol{Y}$ and the filters $H, G, H^*(\omega), G^*(\omega)$ are all designed in the frequency domain. LPS and HPS refer to the low pass and high pass re-scaling operations in the frequency domain where $\beta = 2/(Q+1)$ and $\alpha = 1 - \beta/r$.

2. The forward transform is implemented by iteratively applying a multi-rate two-channel filter bank on the low-pass channel. Figure 4 illustrates the iterated filter bank structure where the output of the low-pass channel is input into a second two-channel filter bank and so on. This is repeated J times for a J-stage wavelet transform or J *levels of decomposition*. In this figure, $H(\omega)$ and $G(\omega)$ represent the analysis low-pass and high-pass filters, respectively.

3. At each level of decomposition, the sampling frequency of the decomposed signal is changed accordingly - the low-pass and high-pass components have sampling rates of αf_s and βf_s respectively, with f_s being the sampling rate of the input signal $(\alpha, \beta < 1)$. In this scheme, the low-pass and high-pass filters H, G can be considered as the anti-
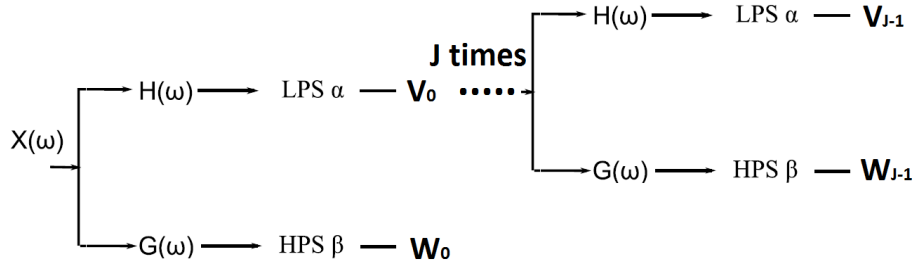
Figure 4: *Iterated filter bank implementation for computing the forward TQWT, given the pre-designed iterated low-pass and high-pass filters $H(\omega)$, $G(\omega)$, respectively.*

aliasing filters[1]. Thus, they are designed such that the filtering operation by H together with the low-pass scaling (LPS) preserves the low-frequency content of the signal, and the filtering operation by G together with the high-pass scaling (HPS) preserves the high frequency content of the signal (terms near Nyquist) with the new sampling rates at each channel being set as mentioned earlier.

4. Figure 5 shows the normalised frequency responses of $H_0(\omega)$ and $G_0(\omega)$ illustrating the behaviour of the first-stage filter bank ($J = 1$). The wavelet transform (or sub-band decomposition) is computed such that for a given input signal $\boldsymbol{X}$, the high-pass sub-band output $\boldsymbol{W_0}$ represents the wavelet coefficients corresponding to high frequency terms from $\alpha f_s/2$ to Nyquist frequency ($f_s/2$) of the input signal.

   $\boldsymbol{V_0}$ contains the low-pass sub-band coefficients from DC to approximately $\alpha f_s/2$ as shown in Figure 5. From here we can repeat this logic for the second stage, where the signal with low-pass frequency response, $\boldsymbol{V_0}$, is input into the second stage. Since the sampling rate at this stage is αf_s, the filters H, G are redefined to have the frequency response from $[0, \alpha^2 f_s]$ (corresponding to $\boldsymbol{V_1}$) and $[\alpha^2 f_s, \alpha f_s]$ (corresponding to $\boldsymbol{W_1}$), respectively. Again, the output of this stage $\boldsymbol{V_1}$ will be fed into the next stage of decomposition.

   Note that $\boldsymbol{W_1}$ (the output of the second stage high-pass filtering) contains the *band-pass* sub-band coefficients with respect to the input $\boldsymbol{X}(\boldsymbol{\omega})$.

5. Using the definitions of α and β and Figure 5 as a visual guide, the values of Q and r affect the wavelet decomposition in the following way: (a) The Q-factor determines the frequency extent of $H(\omega)$, with large values giving a narrower response, (b) the r-parameter determines α or the filter 'roll-off' amount. For larger values of r, the roll-off is more gradual and so $H(\omega)$ and $G(\omega)$ have a greater overlap leading to redundant coefficients.

The wavelet coefficient vector is the concatenation of sub-band vectors

$$\mathbf{w}^T = \begin{bmatrix} DFT^{-1}\{\mathbf{V_{J-1}}\} & DFT^{-1}\{\mathbf{W_{J-1}}\} & \cdots & DFT^{-1}\{\mathbf{W_0}\} \end{bmatrix},$$

where $DFT^{-1}\{.\}$ represents the inverse discrete Fourier transform operation. If the input signal $\boldsymbol{X}$ is the DFT of an impulse function $\delta[n]$, the level 1 decomposition result, $\boldsymbol{W_0}$, will represent the frequency response at *sub-band 1* as similar to that shown in Figure 2(a).

---

[1]Reducing of sampling frequency will result in aliasing, the filters H, G can act as the anti-aliasing filter

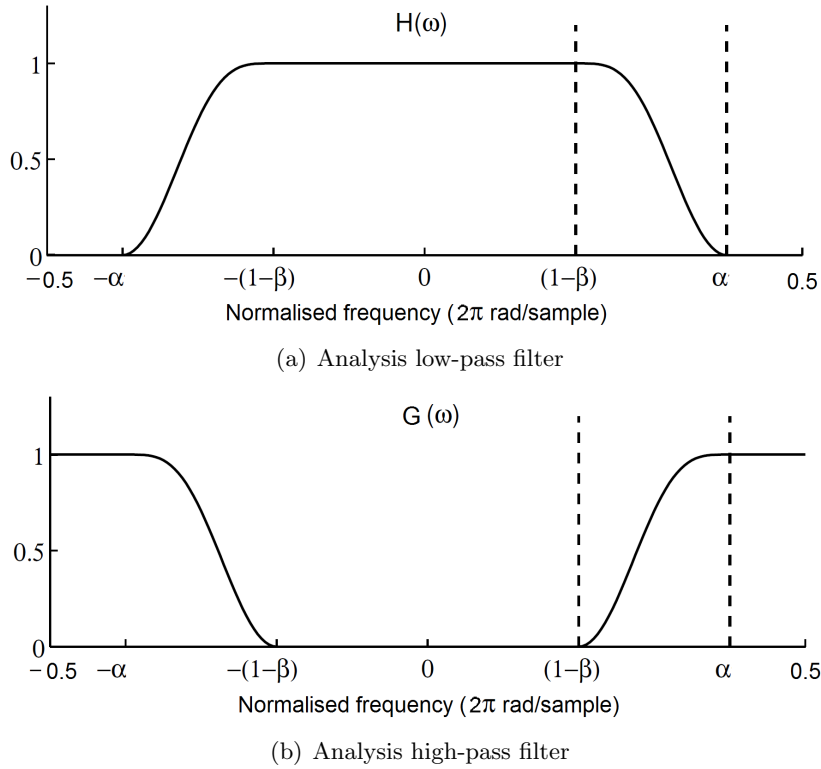(a) Analysis low-pass filter

(b) Analysis high-pass filter

Figure 5: The normalised frequency responses of $H_0(\omega)$ and $G_0(\omega)$ illustrating the behavior of the first-stage filter bank $(J = 1)$.

The inverse Fourier transform of $\boldsymbol{W_0}$ will correspond to the mother wavelet $\psi_{1,0}$ in expression (3). If $\boldsymbol{X}$ is the DFT of delayed impulse $\delta[n-1]$, $\boldsymbol{W_0}$ will represent the response at the same frequency band as the previous, however the associated time domain $DFT^{-1}\{\boldsymbol{W_0}\}$ will correspond to the time translated version of $\psi_{1,0}$ becoming $\psi_{1,1}$ as described in (3).

Similarly, the second level of decomposition of an input impulse signal, $DFT^{-1}\{\boldsymbol{W_1}\}$, will give the $\psi_{2,0}$ mother wavelet function. The father wavelet function ϕ_0 is given by $DFT^{-1}\{\boldsymbol{V_{J-1}}\}$, given that an impulse input signal is used.

2.2 Basis Pursuit Denoising with the TQWT

Consider again a complex signal $\boldsymbol{x}$, represented by a $N \times 1$ column vector. If a linear operation

$$WT : \mathbb{C}^{N \times 1} \to \mathbb{C}^{M \times 1}, \ \text{ for } M > N,$$

represented by the $M \times N$ matrix $\boldsymbol{\Phi}$, is said to sparsely represent the signal $\boldsymbol{x}$, then the corresponding coefficient vector

$$\boldsymbol{w} := WT\{\boldsymbol{x}\}$$

should be sparse, i.e., having a small number of coefficients with high magnitude whilst the remaining coefficients are small and negligible.

The technique of Basis Pursuit Denoising (BPD, or BPDN), first discussed in [43] provides a good platform for the optimisation of the sparse representation of the signal $\boldsymbol{x}$ in the new space WT. The BPD technique is formulated as:

$$\min_{\boldsymbol{w}} \left\{ \|\boldsymbol{x} - \boldsymbol{\Psi w}\|_2^2 + \theta \|\boldsymbol{\lambda} \odot \boldsymbol{w}\|_1 \right\}, \tag{4}$$

where $\|\cdot\|_1, \|\cdot\|_2$ represent the l_1 and l_2 norms, respectively[2]; $\odot$ represents the Hadamard (element-wise) multiplication, $\boldsymbol{\lambda}$ is the compensation vector for sub-band energy gained at each decomposition level due to the scale dependent norm of the TQWT. This means each wavelet coefficient is compensated by the energy of the corresponding wavelet function through the elements of the $\boldsymbol{\lambda}$ vector,

$$\lambda_j = \frac{1}{\|\psi_{j,*}\|_2}, \quad j = 1, 2, \ldots, J. \tag{5}$$

with $\psi_{j,*}$ being a row vector representing the discrete wavelet function (at any time translation) as described in (3). The parameter θ represents the weight which determines the desired energy ratio between the l_1 sparsity component and least square error term (regularisation factor).

The BPD problem described in (4) is a convex problem, and a fast iterative algorithm to solve this problem has been reported by Afonso *et al.* [44], known as the 'Split Augmented Lagrangian Shrinkage Algorithm' (SALSA). For completeness, the algorithm is summarised in Algorithm 1.

Algorithm 1 SALSA Algorithm

1: **procedure** BASIS PURSUIT DENOISING $\boldsymbol{w} = \text{BPD}(\boldsymbol{x}, \boldsymbol{\Phi}, \boldsymbol{\Psi}, \theta, \boldsymbol{\lambda}, \mu)$
2:     Initialisation $\boldsymbol{T} = \theta \boldsymbol{\lambda}/(2\mu), \boldsymbol{u} = \boldsymbol{0}, C = 1/(\mu + 1), d = 0, \boldsymbol{w} = \boldsymbol{\Phi x}$
3:     **for** iteration $k = 1 : P$ **do**
4:         $\boldsymbol{u} = \text{SOFT}(\boldsymbol{w} + \boldsymbol{d}, \boldsymbol{T}) - \boldsymbol{d}$
5:         $\boldsymbol{d} = \boldsymbol{\Phi}(C\boldsymbol{x} - C\boldsymbol{\Psi u})$
6:         $\boldsymbol{w} = \boldsymbol{d} + \boldsymbol{u}$
7:     **end for**
8: **end procedure**
9: **procedure** SOFT THRESHOLDING $\boldsymbol{y} = \text{SOFT}(\boldsymbol{x}, \boldsymbol{T})$
10:     **for** each element index k of vector $\boldsymbol{x}$ **do**
11:         $\boldsymbol{y}_k = \max(|\boldsymbol{x}_k| - \boldsymbol{T}_k, 0)$
12:         $\boldsymbol{y}_k = \boldsymbol{y}_k \boldsymbol{x}_k / (\boldsymbol{y}_k + \boldsymbol{T}_k)$
13:     **end for**
14: **end procedure**

For our processing, the μ parameter is a user-defined step-size in the optimisation set to $\mu = 1$ and $P = 50$ is the number of iterations.

The redundancy parameter r featured in the wavelet transform TQWT allows a non-uniqueness of the solution to represent the signal $\boldsymbol{x}$ in the wavelet domain. The optimisation expressed by (4) yields a way to optimise the solution for the sparse representation of $\boldsymbol{x}$ in the WT domain, i.e., the minimum l_1 norm $\|\boldsymbol{w}\|_1$, whilst minimising the least square error given by $\|\boldsymbol{x} - \boldsymbol{\Psi w}\|_2^2$.

---

[2] l_1 norm of a vector $\boldsymbol{w}$ is given by $\sum_k |\boldsymbol{w}[k]|$, whilst the l_2 norm is computed as $(\sum_k |\boldsymbol{w}[k]|^2)^{1/2}$

2.3   Proposed Algorithm for Rotor Blade Separation

Our proposed scheme for separating the components consists of three successive processing stages: 1) pre-processing; 2) main rotor processing, and 3) tail rotor processing. Processing for the main rotor is carried out first since the main rotor returns are usually stronger than the tail rotor return.

Stage 1 – Pre-Processing

1. The original signal $\boldsymbol{x_{org}}$ is Doppler shifted to remove any component of translational motion of the helicopter. The helicopter body and low-frequency hub components are attenuated by a 256-tap high-pass FIR filter with a cut-off frequency of $PRF/50$. The signal after filtering is denoted by $\boldsymbol{x}$.

2. The signal is decomposed into the positive and negative Doppler frequency components $\boldsymbol{x}_p$ and $\boldsymbol{x}_n$. The processing is applicable to both main and tail rotors, and is described in detail as follows.

   Suppose $\boldsymbol{X} = \mathcal{DFT}\{\boldsymbol{x}\}$ denotes the discrete Fourier transform of time-domain signal $\boldsymbol{x}$. Then, one can write

   $$\boldsymbol{X} = [\boldsymbol{X}_n \ \ \boldsymbol{X}_p]$$

   where $\boldsymbol{X}_n$ and $\boldsymbol{X}_p$ are the Fourier coefficients of the negative and positive frequency components. The time signal becomes $\boldsymbol{x} = \boldsymbol{x}_n + \boldsymbol{x}_p$, with the components given simply as

   $$\boldsymbol{x}_n = \mathcal{DFT}^{-1}\{[\boldsymbol{0} \ \ \boldsymbol{X}_n]\}, \ \ \boldsymbol{x}_p = \mathcal{DFT}^{-1}\{[\boldsymbol{X}_p \ \ \boldsymbol{0}]\},$$

   Here, $\mathcal{DFT}^{-1}\{.\}$ represents the inverse discrete Fourier transform. This processing applies to both main and tail rotors, and the components will be processed separately in the next stages.

Stages 2 - Main Rotor Blade Processing
Two sub-stages are involved:
Stage 2.1:

1.1 For the given set of (Q, r, J), compute the compensation vector $\boldsymbol{\lambda}$ for the wavelets ψ_j for all scales, based on (5). Set the weighting parameter θ which has been empirically found to range between 1 and 2.

1.2 Apply the BPD algorithm as described in Section 2.2 and the SALSA Algorithm to solve the optimisation problem of (4).

   This yields the weight vector output denoted as $\hat{\boldsymbol{w}}_{BPD}$, and is given by

   $$\hat{\boldsymbol{w}}_{BPD} = \arg\min_{\boldsymbol{w}} \left\{ \|\boldsymbol{y} - \boldsymbol{\Psi}\boldsymbol{w}\|_2^2 + \theta\|\boldsymbol{\lambda} \odot \boldsymbol{w}\|_1 \right\}, \tag{6}$$

   where $\boldsymbol{y}$ may be $\boldsymbol{x}_n$, or $\boldsymbol{x}_p$, or their residual (remnant) component.

Stage 2.2:
Apply the Reweighted l_1 Minimisation algorithm, as shown in Algorithm 2, to re-evaluate the coefficients of the wavelets determined in stage 2.1. The weight vector output from this processing is denoted as $\boldsymbol{w}_{reweighted}$.

Stages 3 - Tail Rotor Blade Processing
The residual signal after main rotor blade processing is input to Stage 3. The same processing is used to separate the tail rotor blade component, denoted as *Stage 3.1* and *Stage 3.2*, except that the wavelet parameters are tuned differently for this component. The residual signal after Stage 3 is expected to consist mostly of remaining components from the body (including the rotor hubs) and interference, as expressed by equation (1).

Algorithm 2 Re-Weighted l_1 Minimisation

1: Construct the re-weighted matrix $\boldsymbol{W}$ as a diagonal matrix with diagonal values given by $\hat{\boldsymbol{w}}_{BPD}$, as

$$\boldsymbol{W}_{\{k,k\}} \quad = \quad \frac{1}{|\hat{\boldsymbol{w}}_{BPD}[k]| + \epsilon}, \quad k = 1, \ldots, M; \tag{7}$$

$$\boldsymbol{W} \quad \leftarrow \quad \frac{\boldsymbol{W}}{\max\{|\boldsymbol{W}|\}}; \quad \text{(normalisation)} \tag{8}$$

2: Solve the re-weighted BPD algorithm

$$\hat{\boldsymbol{w}}_{reweighted} = \arg \min_{\boldsymbol{w}} \left\{ \|\boldsymbol{y} - \boldsymbol{\Psi}\boldsymbol{w}\|_2^2 + \theta\|\boldsymbol{W}\boldsymbol{\lambda} \odot \boldsymbol{w}\|_1 \right\}, \tag{9}$$

where the other parameters are as defined in (6).
3: The reconstructed signal after the re-evaluation is given by $\boldsymbol{\Psi}\,\hat{\boldsymbol{w}}_{reweighted}$.

The following points should be noted of the proposed algorithm.

1. The positive and negative Doppler frequency components of the composite signal are processed separately to mitigate artifacts caused by mirror image effects of the signal frequency spectrum. For example, if there exists a strong component of interest on one side of the spectrum that is picked up by the algorithm, the nature of the TQWT is such that a smaller magnitude mirror image component of opposite frequency may also be extracted. Processing only a one-sided spectrum at a time ensures that any component formed on the other side of the spectrum is an artifact caused by mirror effects, which can then be filtered out.

2. The refinement processing with the Reweighted l_1 Minimisation has been noted to significantly enhance the performance of the algorithm by moving the l_1 solution toward an ideal and sparse l_0 solution, where only a few coefficients are non-zero.

3. Parameter θ is empirically chosen based on the relative energy between the component of interest and the other components which are treated as interference for this extraction problem. It starts from 2 for a normalised input, reducing by 0.1 until all blade components are extracted by sub-stages 2.1 and 3.1.

4. Parameter ϵ is a few orders of magnitude smaller compared to $\hat{\boldsymbol{w}}_{BPD}$; it serves as a means to avoid division by zero.
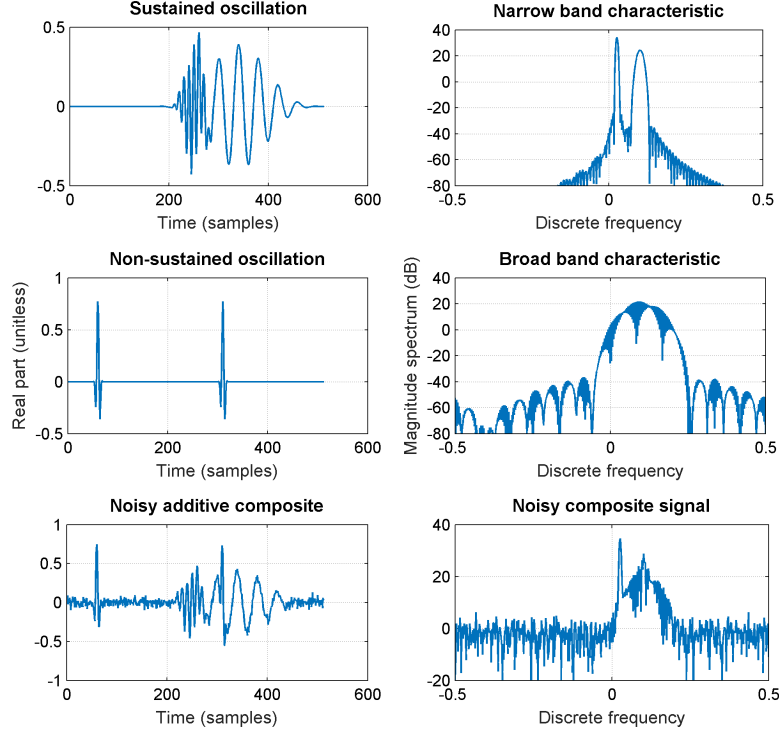
Figure 6: The synthetic sinusoid signals: Top panels represent the sustained oscillation (left) and its corresponding narrow band spectrum (right); middle panels illustrate the non-sustained (left) and corresponding broad band spectrum (right), the noisy composite signal is shown in the bottom panels, time domain (left) and magnitude spectrum (right).

2.4   An example for technique demonstration

To demonstrate the use the proposed algorithm for signal separation exploiting the sparsity of the components, the following example is considered. Let the signal $\boldsymbol{x}$ be an additive composition of a broadband component $\boldsymbol{x_b}$ (non-sustained oscillation with low Q resonance), a narrowband component $\boldsymbol{x_n}$ (sustained oscillation with high Q resonance) and white Gaussian noise $\boldsymbol{n}$, given by

$$\boldsymbol{x} = \boldsymbol{x_b} + \boldsymbol{x_n} + \boldsymbol{n}. \tag{10}$$

The time domain signals and their associated magnitude spectra are illustrated in Figure 6 for individual components and the composite signal. The key challenges for the separation of these components are signal components overlap in both time and frequency, and no prior knowledge of the timing of appearance of the components is available. Thus, conventional filtering methods cannot be applied.

After applying the proposed signal separation method, we successfully extract the broadband component $\boldsymbol{x_b}$ as shown in Figure 7. The TQWT and its associated dictionary matrix Φ are chosen such that the broadband spectral characteristics can be sparsely represented. This example demonstrates how the proposed technique can be used to extract wideband impulsive
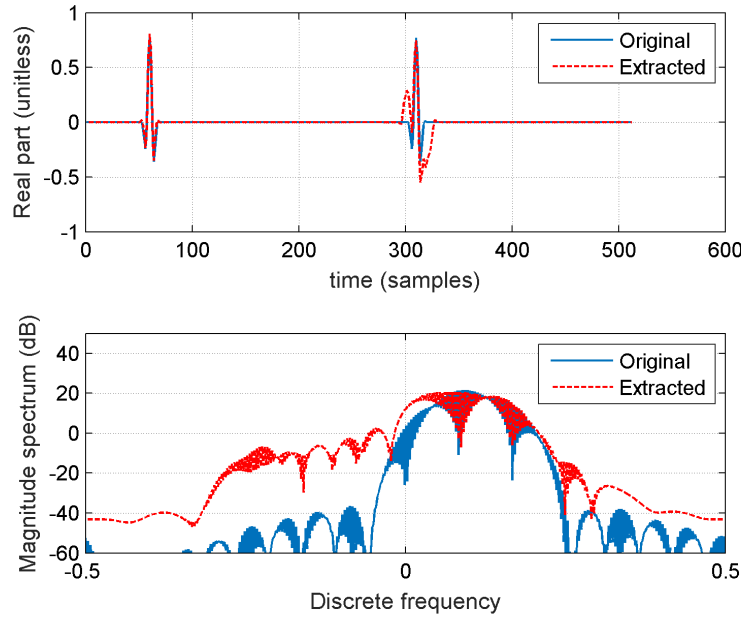
*Figure 7:   The broad band component extraction using the proposed approach.   Top panel
illustrates the real part of the original (solid blue) and the extracted signals (dashed
red) whilst bottom panels are for the associated magnitude spectrum (same color
scheme applied).*

signal (similar to radar return from a helicopter blade) when mixed with narrowband sustained
signals (similar to radar returns from helicopter body and hub components).

3   Demonstration with Simulated Data

The algorithm proposed in Section 2.3 is first demonstrated with simulated data of a hovering
helicopter (no translational motion). The target model consists of three components: main
rotor blades, tail rotor blades, and the rotor hub and body. The main rotor is made up of
3 radial wires, each having a length of 5 m, and rotating at 390 RPM. The blade tip is also
modelled using a point scatterer model to give the blade tip a return over a small angular
extent. The tail rotor is modelled with 2 radial wires rotating at 3000 RPM, each having
a length of 0.9 m. The main rotor hub is modelled simply as a band-limited (± 2.5 kHz)
Gaussian noise source, while a large 'DC term' represents the helicopter body return.

The radar is modelled as a pulse-Doppler radar operating at 9.5 GHz (X-band) and using a
PRF of 66.7 kHz, collecting a single sample per pulse (without any pulse compression) at the
range gate where the target is isolated. Dwell time on the target is 150 ms in duration, which
is approximately a complete rotation of the main rotor. Figure 8 shows the spectrograms of
the signals before and after the first stage of pre-processing.

It should be noted that although this section is dedicated to processing simulated data, the
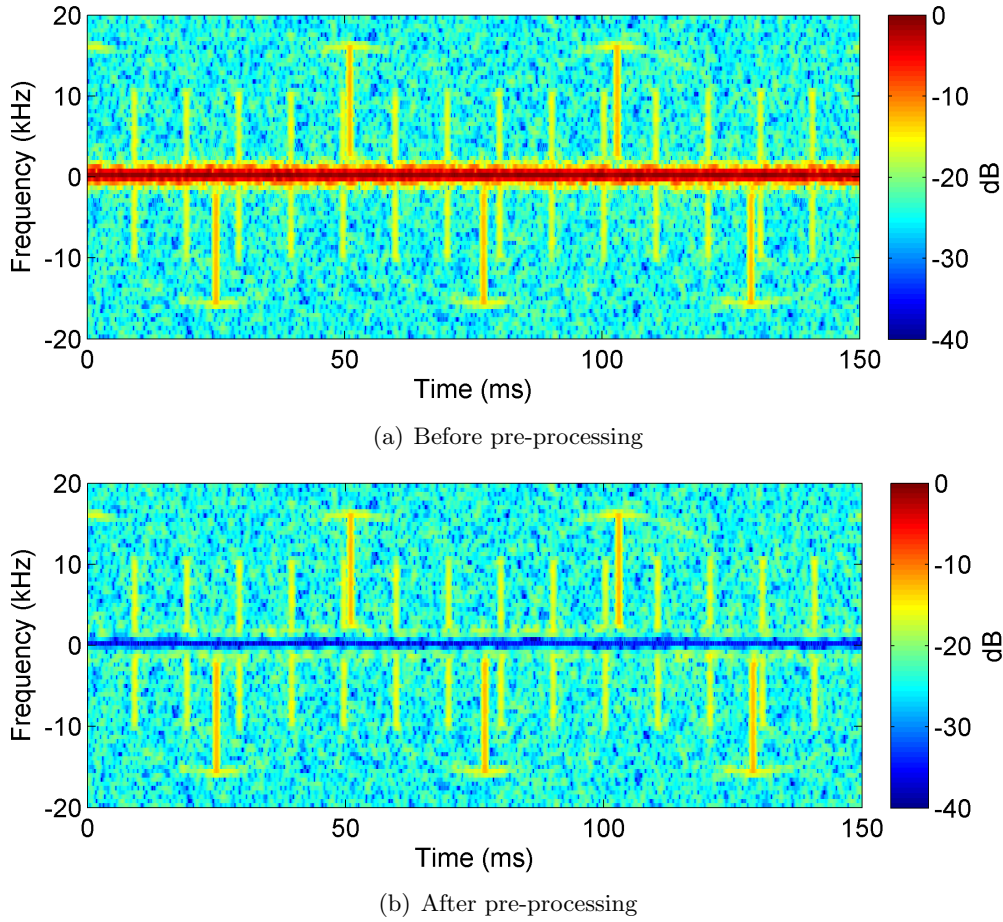
(a) Before pre-processing

(b) After pre-processing

Figure 8: Stage 1 - pre-processing of simulated data at X-band.

wavelet parameters used and any modification to the processing stages that occur, are in preparation for real data which is presented in the next section. References to this fact are highlighted in the subsections below.

3.1 Main Rotor Blade Separation

For the main rotor blade signal separation, we apply Stage 2 of the algorithm. The TQWT wavelet coefficients are determined using the following parameters: $Q = 6, r = 25$, and $J = 40$. A discussion on the selection of these parameters is reserved for Section 3.4.

Let $\hat{\boldsymbol{x}}_{MB}$ be the complex signal representing the estimated and extracted component produced by the main rotor processing, with the residual signal expressible as

$$\boldsymbol{x}_{res} = \boldsymbol{x} - \hat{\boldsymbol{x}}_{MB}.$$

The spectrograms of the extracted main rotor component and the residual signal immediately after the Stage 2.1 of the algorithm, are shown in Figure 9(a) and Figure 9(b) respectively. Note that the processing at this stage correctly extracts the wavelet components but not their
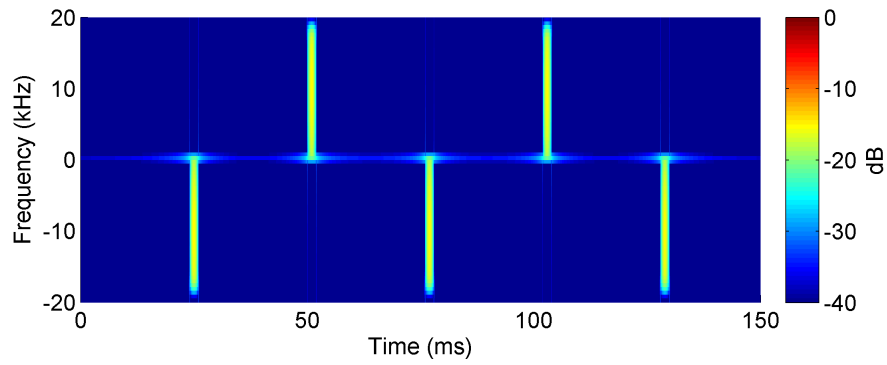
(a) Extracted main blade component after stage 2.1 processing
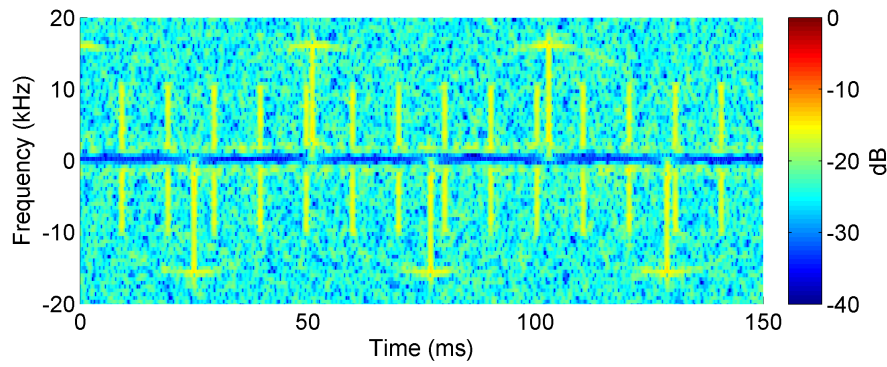
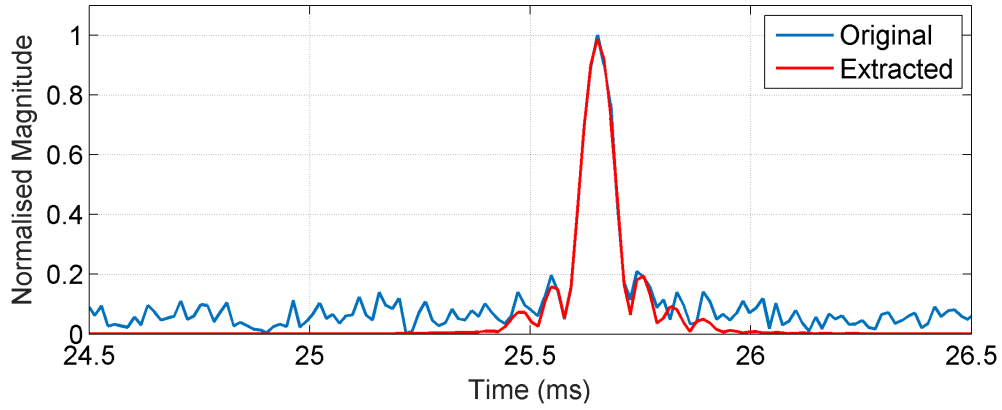(b) Residual signal after stage 2.1.
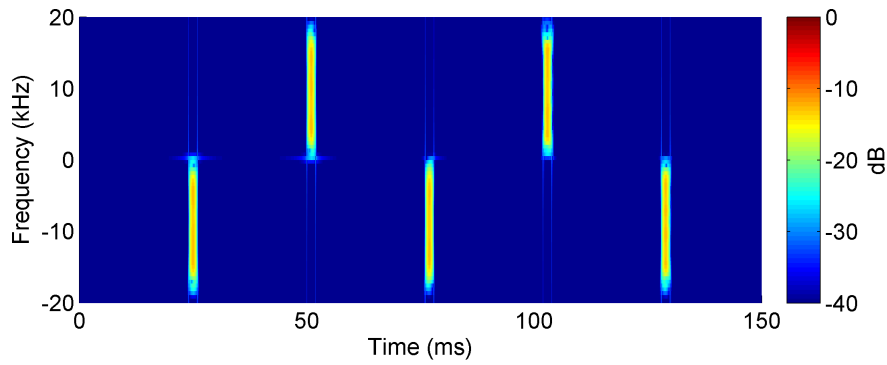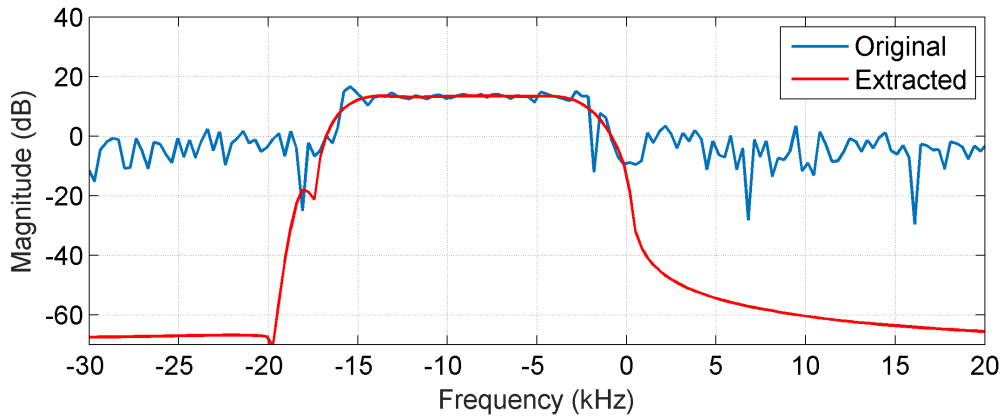

(c) Extracted component after stage 2.2 processing
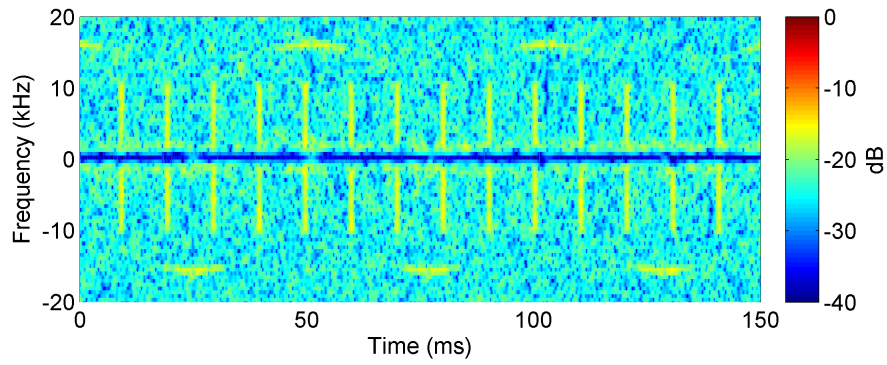
(d) Residual signal after stage 2.2.

Figure 9: Simulated results in Stage 2 of the algorithm, for main rotor processing.

(a) Time signal of the first receding main blade

(b) Spectrum of the first receding main blade

Figure 10: Original and reconstructed signals after stage 2.2 of (a) the first receding main blade in time domain; and (b) the same signals in the frequency domain.

coefficients. As a result, only part of the signal energy is extracted, with a significant amount of energy from the main blades still observable in the residual signal shown in Figure 9(b).

In Stage 2.2 of the algorithm, the application of the Re-weighted l_1 Minimisation re-evaluates the weight vector, which fully extracts the signal components of interest thus minimising errors that could have propagated, or even been amplified, further down the processing chain. The improved extracted components are shown in Figure 9(c), which in this case are stronger than that in Figure 9(a). Figure 9(d) shows the spectrogram of the residual signal after Stage 2.2, where only the tail blade components and some of the energy of the main blade tips remain.

To further highlight the effectiveness of the proposed algorithm, data from around the first receding blade flash (negative Doppler) is presented in Figure 10. Figure 10(a) shows a comparison between the original and the final extracted component in the time domain, while Figure 10(b) shows the same signal but in the frequency domain. Excellent agreement is clearly observable in both time and frequency domains. A similar performance has been observed for approaching blade flashes (positive Doppler) as well.

3.2 Tail Rotor Blade Separation

For the tail rotor blade signal separation, we apply Stage 3 of the algorithm. The residual signal output from the main rotor processing is the input to the tail rotor processing; the wavelet coefficients are estimated using a different set of wavelet parameters: $Q = 1.2$, $r = 20$, and $J = 17$. Again, a discussion on the selection of these parameters is reserved for Section 3.4.

Unlike the main blade and low frequency rotor hub components, the tail blade components are usually significantly weaker in magnitude. For real data, bright specular returns in the low-frequency part of the main rotor spectrum interferes with the TQWT processing for tail rotor blade extraction. To overcome this, the algorithm in Stage 3.1 is modified to allow the bandwidth of the father wavelet to be user-defined so that strong specular components from the main rotor hub are spanned by the sub-band of the father wavelet. Then, to avoid capturing these components, the compensation factor for the father wavelet coefficient, λ_{J+1}, is set to a large value – 1000 times that determined in the SALSA algorithm. This effectively means that components in the low-pass sub-band of the father wavelet will not be extracted unless they exceed 60 dB above components in other sub-bands.

Here, the user-defined father wavelet bandwidth has a frequency extent in the range ± 6 kHz, which is set to a value larger than the hub frequency extent to allow for filter roll-off. Using this requirement on the father wavelet, the J parameter is calculated[3] with $Q = 1.2$ and $r = 20$.

Although this section is dedicated to simulated data and bright specular returns in the rotor hub do not exist, the same processing for both real and simulated data is used to maintain consistency and so that the modification of the father wavelet compensation factor can be tested using the ideal simulated case.

The result of the tail blade extraction after Stage 3.2 optimisation, and after the modification to the compensation vector, is shown in Figure 11(b). For convenience, the signal in Figure 9(d) is re-shown in Figure 11(a).

The full energy of the tail blade components have been extracted as compared to that in Figure 11(a). It shows that the algorithm is capable of separating tail rotor blade returns from hub and main body, after main rotor blade signal separation. The residual signal is shown in Figure 11(c) showing the absence of main and tail rotor blade returns. The residual signal only shows the hub components and the return from main blade tips.

Again, the extracted signal is observed in the time and frequency domain. The extracted time-domain magnitude of the first observed tail blade is shown in Figure 12(a), and the corresponding Doppler spectrum is shown in Figure 12(b).

Good extraction of the tail blades can be observed in which only the component of interest is extracted to approximate the original signal whilst rejecting the other components. One can argue that since the hubs and the tail blades components are well separated in the frequency domain, linear band-pass filtering can be used to extract the tail signal. However, if linear filtering is used, unwanted components, such as noise and other residue, exist in the pass-band region of the filter at times other than when the tail rotor blades occur. In Figure 11(b), the

---

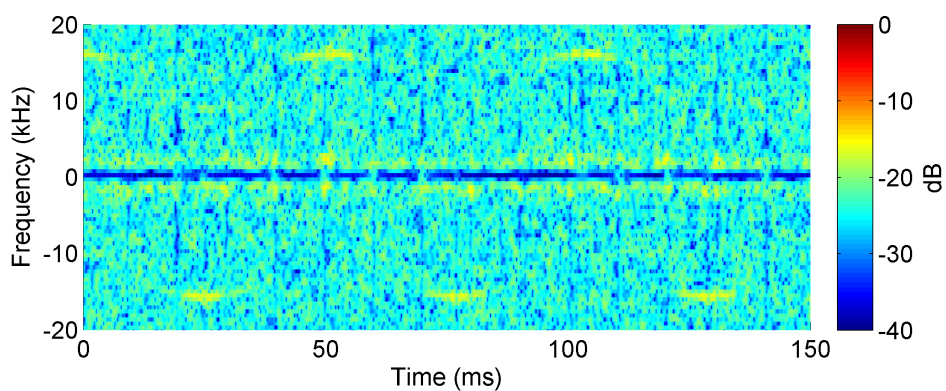[3]An automated algorithm is implemented to compute J given (Q, r) and the low-pass spectrum spread.

(a) Spectrogram after main blade extraction (tail return only)

(b) Extracted tail components after 2nd stage processing
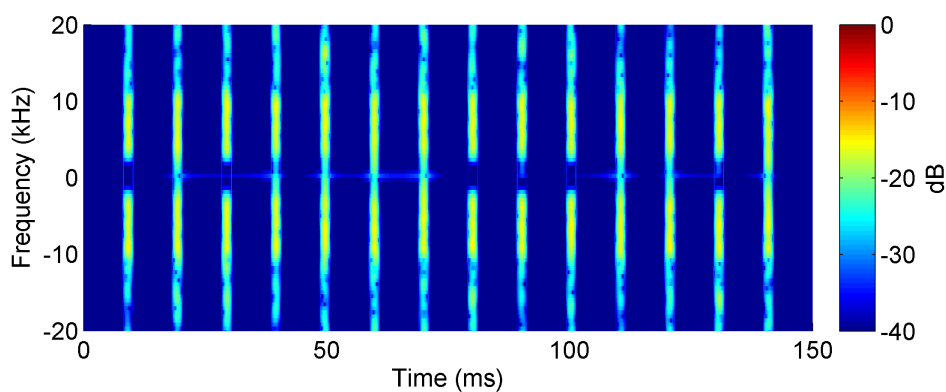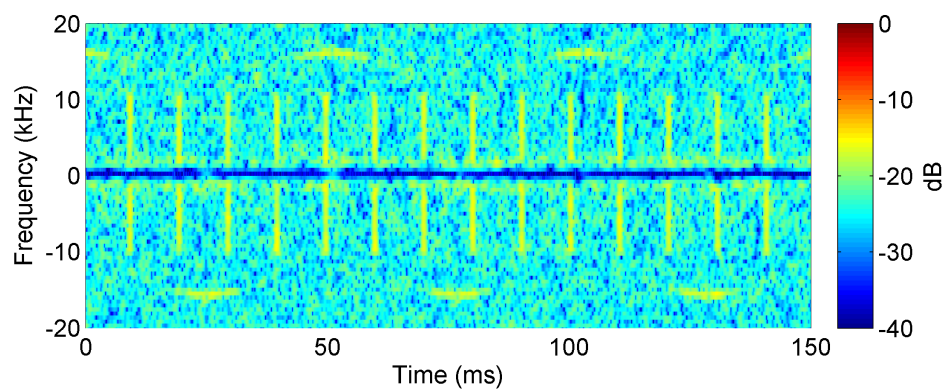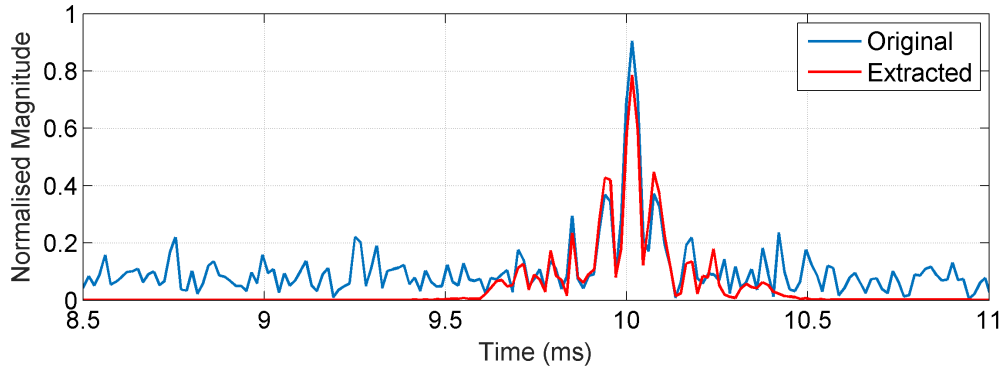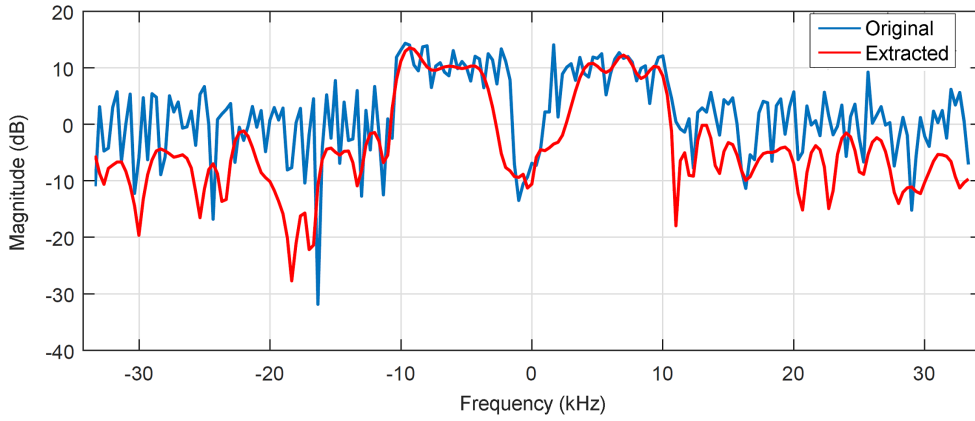

(c) Residual signal after tail extraction

Figure 11:   Simulated results in Stage 3 of the algorithm, for tail rotor processing.

(a) Time-domain signals of the first tail flash

(b) Frequency-domain signals of the first tail flash

Figure 12: Comparison of the input and reconstructed signals in Stage 3, for the tail rotor processing.

extracted signal is observed to have energy only at the times the tail blades are viewed by the radar whilst rejecting energy at other times.

In Figure 12(b), it should be noted that the low frequency terms near DC in the spectrum of the separated tail signal was not effectively extracted due to the modification of the compensation factor λ_{J+1} as discussed earlier. The father wavelet bandwidth can be reduced to enable the extraction of more low-pass information from the tail blades, however a trade-off needs to be made since this can potentially result in a failure to extract all tail rotor components or extraction of unwanted hub components.

3.3   Main Rotor Blade Separation Under Strong Interference

In this section, we demonstrate a case where noise and helicopter hub returns have a high intensity, thus interference components and main blade signal are overlapped in both time and frequency. This example shows the robustness of the proposed technique to in-band interference and its ability to extract original blade signals with high fidelity features. Figure 13 shows the spectrogram of the original signal before and after pre-processing stages. After ap-

(a) Before pre-processing

(b) After pre-processing
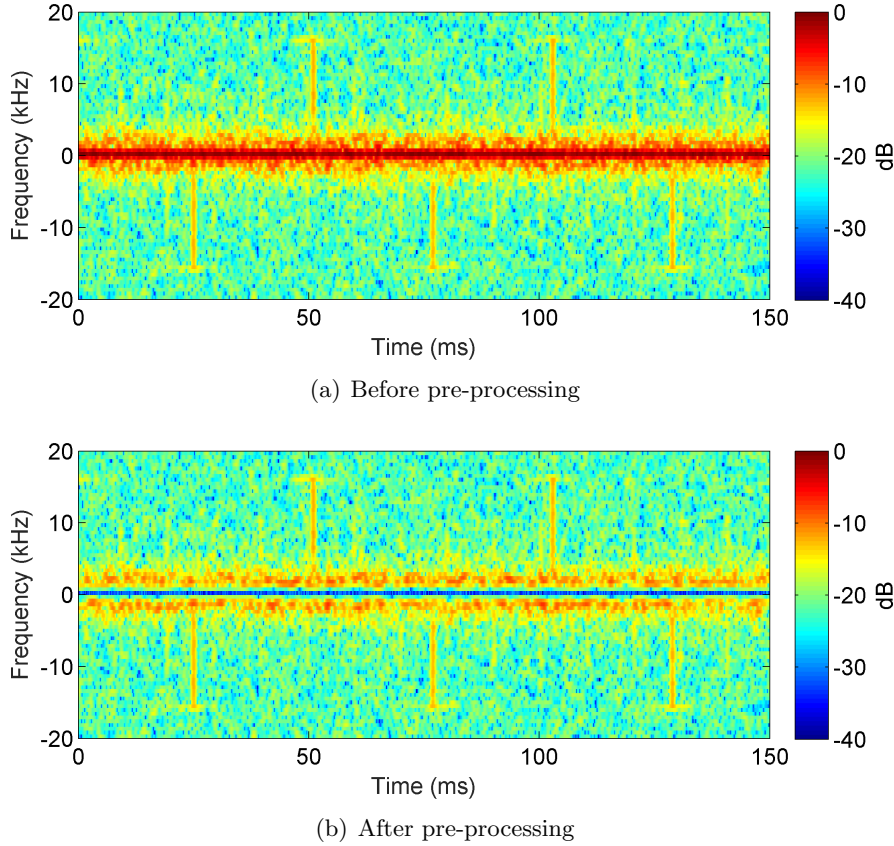
Figure 13: Stage 1 - pre-processing of simulated data at X-band with high level interference.

plying stage 1 and 2 processing, the main blade signal is extracted and the results are shown in Figure 14. Even in the presence of strong interference, the proposed method is capable of accurately extracting the main blade returns as shown in Figure 14(a).

The time and frequency domain plots of the first receding and approaching blades are shown in Figures 15 and 16, respectively. Each plot shows original main blade signal, composite signal, and the extracted main blade signal using the proposed method. In the case of receding blade case (Figure 15(a)), we notice destructive interference where blade return is reduced and its time-domain characteristics have been changed (notice that single peak is split into two sub-peaks). The extracted main blade signal recover the time-domain characteristics of the original signal and more closely matched with the original simulated signal. Obtaining the extracted signal directly in time-domain from the composite signal would not work in this case as time-domain features of the original blade signal have been significantly changed during the composition. From the application point of view, it is important that both time-domain and frequency-domain features are preserved in the extracted signal. Figure 15(b) shows the same comparison in the frequency domain. Low frequency interference components are not present in the extracted signal and also a flatter plateau is observable which is closely matched to the original main blade response.

Figure 16(a) shows the results for the approaching blade case in time domain. Here, the original blade signal is constructively interfered, and composite signal peak has more energy
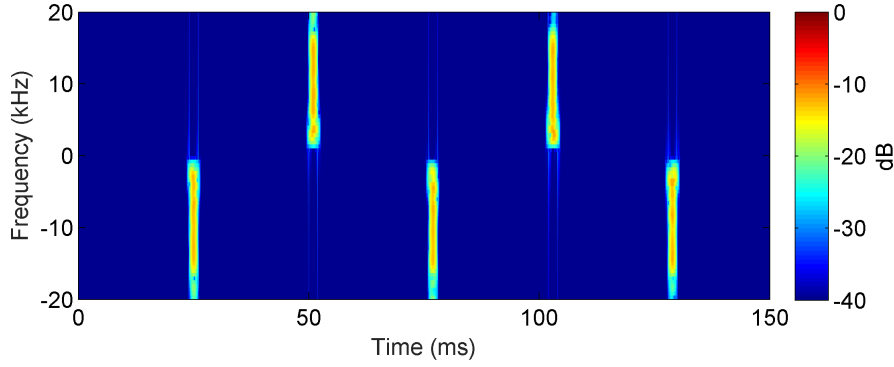
(a) Extracted main blade component in the presence of strong interference
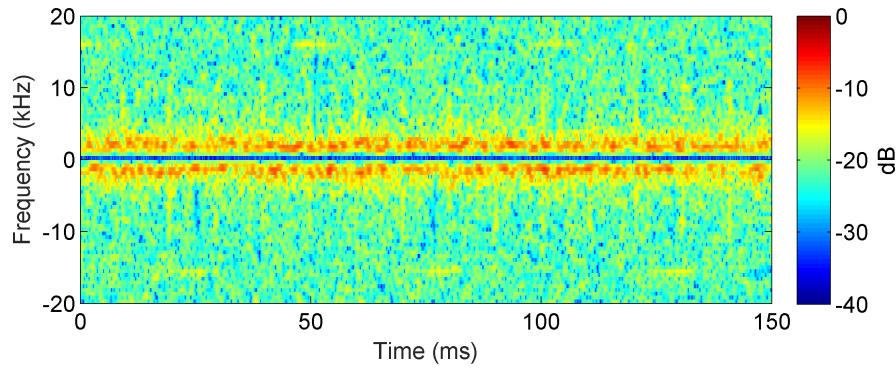
(b) Remnant signal after extraction in the presence of strong interference

Figure 14:   Simulated results for the main blade signal extraction under strong interference.

than that of present in original blade signal. Again, the extracted blade signal using the proposed method is a closer match to the original blade signal compared the composite signal. Figure 16(b) shows the frequency domain comparison. Again, low frequency interference is avoided during the extraction and a similar frequency response to the original blade signal is obtained.

3.4   Optimum Choices of Parameters for the TQWT

For the main rotor blade return, it is desirable to use optimum transform parameters such that the representation of the main blade component in the new domain is sparsest compared to the other components. This was achieved by constructing the TQWT transform matrix Φ for a range of Q-factor values and finding the optimised solutions $\hat{\boldsymbol{w}}_{main}, \hat{\boldsymbol{w}}_{tail}, \hat{\boldsymbol{w}}_{hub}$ for each Q factor. It was found that a value of 6 for the Q-factor gave the sparsest representation for the given r and J parameters.

The redundancy factor r was empirically fixed at 25 to provide sufficient degree of freedom for the optimisation and J was selected such that the spectral bandwidth of the father wavelet spans ± 18 kHz, which is approximately the Doppler extent of the main rotor blades in this simulated example, resulting in a calculated value of $J = 40$. The sub-band decomposition of
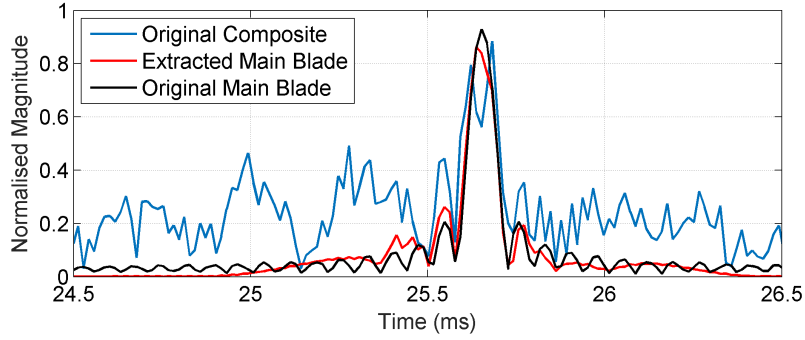
(a) Results for first receding blade in time domain in the presence of strong interference
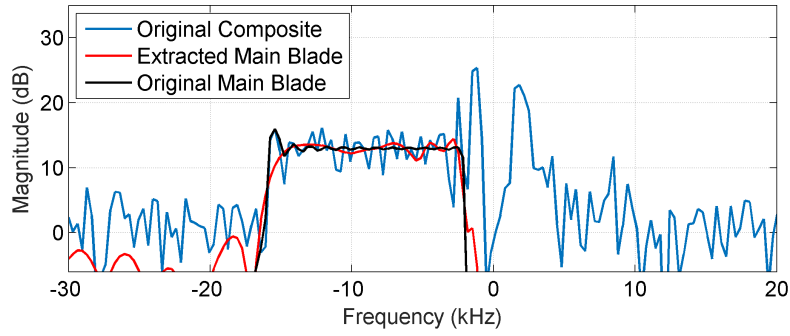
(b) Results for first receding blade in frequency domain in the presence of strong interference

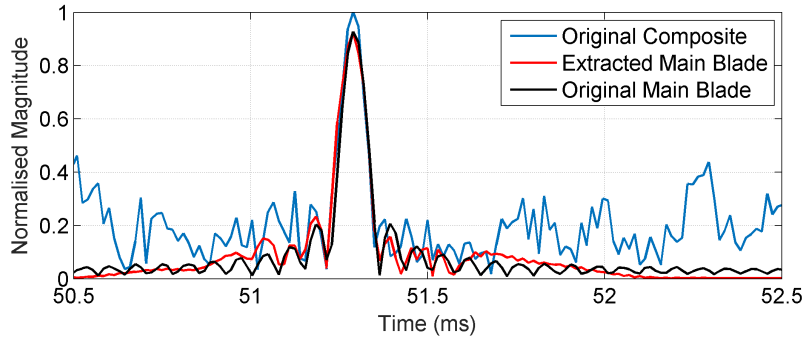Figure 15: *Results for the first receding blade under strong interference.*

the TQWTs associated with this set of Q, r, J parameters is shown in Figure 17(a), plotted for positive Doppler frequencies only.

The following steps were taken to compute J, given Q, r and the spectral bandwidth of the father wavelet required, denoted here by B_{3dB}:

1. Compute low-pass filter $H(\omega)$ and scaling factor α (refer to Figure 4).

2. Compute V_J ($J = 0$ for the first iteration) for an input signal $X(\omega)$ where $X(\omega)$ is the DFT of the impulse signal $x[n] = \delta[n]$.

3. Compute 3dB bandwidth of V_J, denoted by $B_{3dB,J}$.

4. If $B_{3dB,J} > B_{3dB}$, return to Step 2 with $J = J + 1$.

To show sparsity characteristics under the TQWT of the various components of the helicopter signal, Figure 18 is a plot of the magnitudes of $\hat{\boldsymbol{w}}_{main}, \hat{\boldsymbol{w}}_{tail}, \hat{\boldsymbol{w}}_{hub}$, normalised and sorted in descending order. The main blade coefficients are most sparse compared to the other components, with the first 20 coefficients representing most of its signal energy. A similar characteristic can be seen for the tail rotor. The hub component is the least sparse.

However, it should be noted that the main blade returns are stronger in magnitude compared to the tail returns, which is not reflected in the plot in Figure 18 since the weights are normalised. This effectively means that for the same sparsity level, the main blade component

(a) Results for first approaching blade in time domain in the presence of strong interference
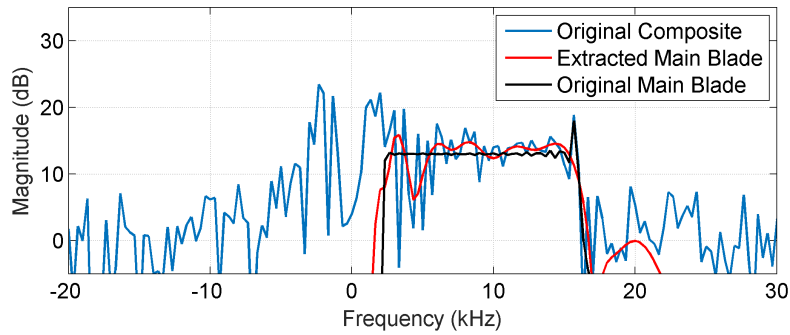
(b) Results for first approaching blade in frequency domain in the presence of strong interference

Figure 16: Results for the first approaching blade under strong interference.

can be expected to be more dominant compared to the tail counterpart. These selected TQWT parameters were used throughout the report for both simulated and real data for main rotor signal separation.

The transform parameters for the tail rotor were chosen so that the following conditions were met: (1) as discussed in Section 3.2, the father wavelet sub-band was designed to occupy the ± 6 kHz part of the spectrum, which is a user-defined parameter; (2) The mother wavelets in the band-pass region of the spectrum is designed to have a broad bandwidth to capture the tail component. Accordingly, a low value of 1.2 for the Q-factor was found to be suitable for the tail rotor processing. Also, setting $r = 20$ gave sufficient redundancy which led to a calculated value of $J = 17$. The sub-band decomposition of the TQWTs associated with this set of Q, r, J parameters is shown in Figure 17(b). Again, these parameters were used throughout the report for tail rotor signal separation.
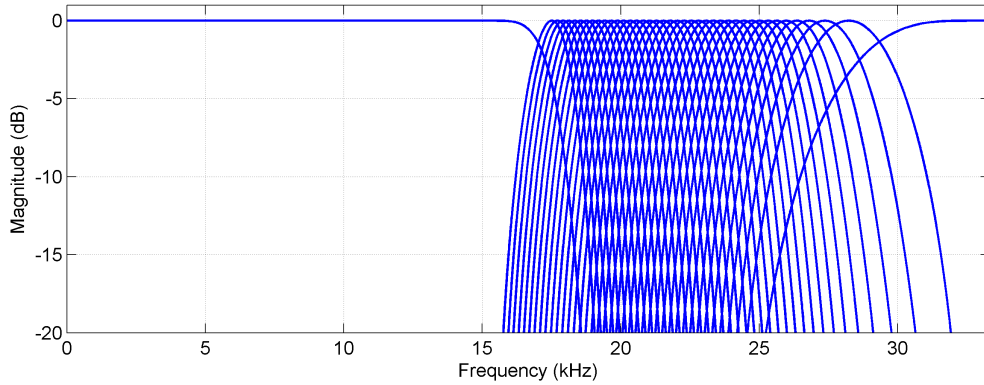
(a) Main blade, Q=6,r=25 and J=40.
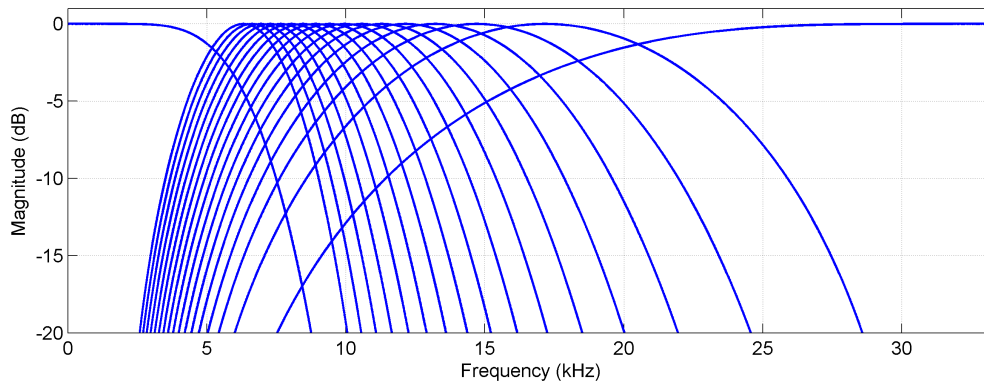
(b) Tail blade processing, Q=1.2,r=20 and J=17.

Figure 17: Sub-band decomposition used in the processing of main and tail rotors

4   Experimental results with real data

The real data used in this report was collected during dedicated helicopter trials held in May 2011. The Defence Science Technology (DST) Group Wandana II van-mounted experimental pulse Doppler radar was used to illuminate a *hovering* Squirrel AS350BA helicopter at various aspect angles ranging from 0 to 180° with 0° aspect relating to the 'nose on' aspect. A photo of the actual helicopter used for the measurements is shown Figure 19. The Squirrel helicopter has 3 main rotor blades and 2 tail rotor blades, which rotate at approximate nominal rotation rates of 394 and 3000 RPM respectively. In this report we use aspect angles of 45° and 180° which provides data that shows both the main and tail rotor blade returns with adequate SNR.

The radar collected measurements at carrier frequencies of 9.5 GHz (X-band) and 16.8 GHz (Ku-band) using a PRF of 66.7 kHz with horizontal polarisation on transmit and receive. A single sample per pulse was collected at the range bin where helicopter was located with no pulse compression.
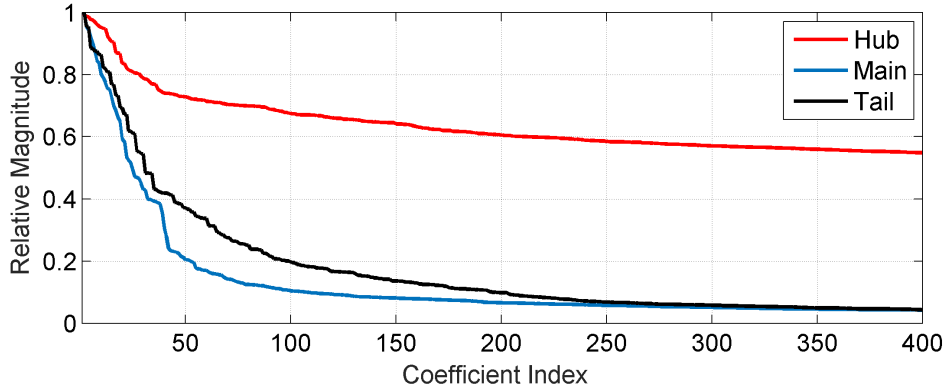
Figure 18: Sorted wavelet coefficients in descending order for $Q = 6, r = 25, J = 40$.

*Figure 19: Photo of the Squirrel AS350BA (Courtesy of Australian Helicopters Pty Ltd)*

4.1 Experimental data at X-band: $45°$ aspect

In this section, we apply the proposed algorithm on the X-band data collected at the aspect angle of $45°$. The spectrogram of the original signal plotted for one revolution of the main blade is shown in Figure 20(a). The spectrogram clearly shows the large return from the helicopter body at 0 Hz (DC), the rotor hub return that has a Doppler frequency extent of approximately ± 3 kHz, the six blade flashes from the three main rotor blades (both positive and negative Doppler frequencies) and the less dominant blade flashes from the 2-bladed tail rotor.

We begin with Stage 1 processing where by the rotor hub and body Doppler frequency terms are filtered out. The high-pass filtered signal is plotted in Figure 20(b). Note that the spectrograms showing processed results in the sections below are normalised to this pre-processed signal.

Stage 2 processing is then applied to the pre-processed data. Effective extraction of the main rotating blades is achieved using the tuned parameters Q, r, J, found based on the simulated data for the X-band signal.

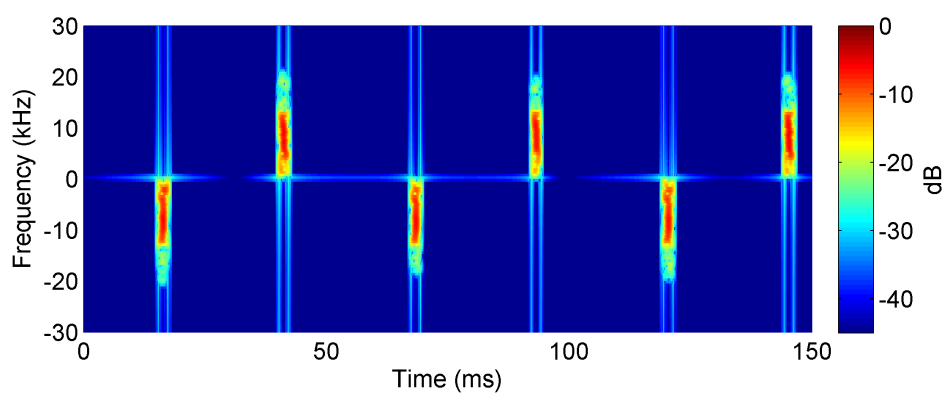In Figure 21(a), the spectrogram of extracted signal after Stage 2.2 processing is shown.
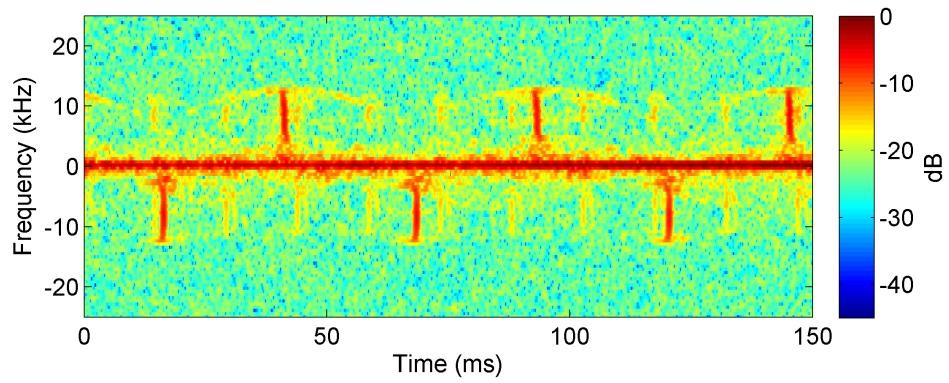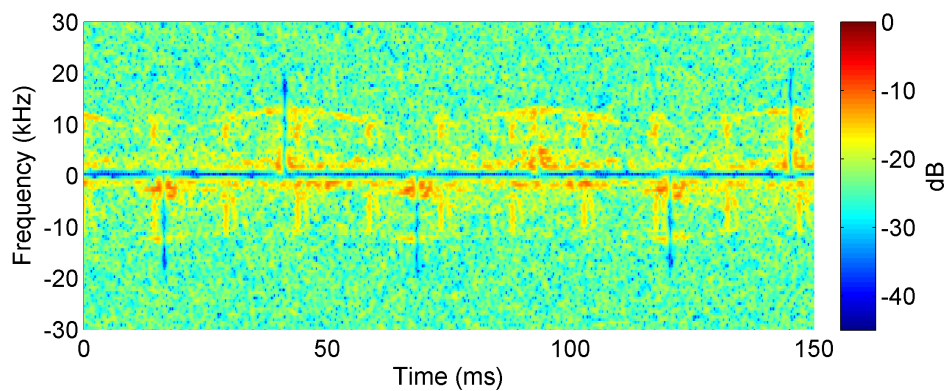
(a) Before pre-processing
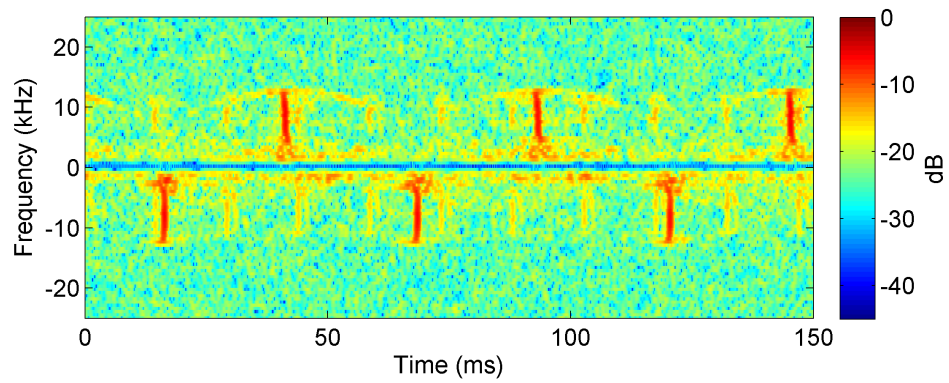
(b) After pre-processing

Figure 20:   One cycle of Squirrel helicopter data at X-band, 45° aspect, in Stage 1.

(a) Extracted main rotor blade components

(b) Residual signal after main blade extraction

Figure 21: Stage 2 processing – for the main rotor blades – on Squirrel helicopter data, at X-band, 45° aspect.

The blade energy corresponding to the six blade flashes are effectively extracted in both the temporal and frequency space. This is seen in the residual signal shown in Figure 21(b).

To further highlight the effectiveness of the blade extraction, the first approaching and the first receding blade flash is plotted in the time and frequency domains. Both the approaching and receding blades are presented because the blade will have different scatterering properties due to the physical construction of the blade and due to the blades aerofoil design.

Figure 22(a) shows a comparison between the original and extracted time-domain signals of the first approaching main blade, after Stage 2.2 processing. The results show very good correlation between the original and extracted signal in both the shape, main-lobe and side-lobe structure, and magnitude of the responses. The frequency response of this first approaching blade flash signal is shown in Figure 22(b). Again, the correlation between the original and extracted signal is very good. The Doppler extent and response shape of the extracted signal is comparable to the original signal, especially the frequency plateau corresponding to the blade response, in the Doppler frequency range between 1 and 12 kHz.

Similarly, Figure 22(c) shows a comparison between the original and extracted time-domain signals of the first receding main blade, after second stage processing. This zoomed in plot highlights how well the BPD processing works on this signal in extracting the main blade response. Again, the frequency response of the receding blade signal, in Figure 22(d), shows the blade plateau region and the correlation between the original and extracted signals.

Stage 3 processing is applied to extract the tail rotor blade return from the residual signal after the main rotor blade extraction. This tail blade only spectrogram is re-shown in Figure 23(a) to provide a visual reference. The tail component can be observed on both sides of the frequency spectrum with each blade producing a flash at the same time, due to the even parity of the tail rotor.

To highlight the inadequacy of using linear filtering for this problem, there are strong unwanted components that fall in the same frequency band as the tail blades signal, (approximately $[5, 12]$ kHz, and $[-12, -5]$ kHz), that interfere with the processing because they are not associated with the tail rotor blade, but may belong to residual energy from the main blade (in particular the main blade tip) or other scattering phenomenon. Hence, linear filtering cannot be used, as these components would be extracted with the tail blade signal.

By using the proposed technique the signal from the tail blade can be extracted, after Stage 3.2 processing and modifying the father wavelet compensation factor, as seen in Figure 23(b). The extracted signal extracts the tail rotor blade signal for the correct Doppler extent and temporal spaces. The residual signal after tail blade extraction is seen in Figure 23(c). When compared to the spectrogram after main blade extraction (Figure 23(a)) the residual spectrogram shows the absence of tail blade energy.

Again, to fully show the effectiveness of the proposed technique, the signal from the first tail rotor blade is plotted in the time and frequency domains. Figure 24(a) shows the comparison between the original and extracted tail blade signal in the time-domain. The two signals are comparable with temporal features extracted correctly. Figure 24(b) shows the comparison between the original and extracted tail blade signal in the frequency-domain. The shape and magnitude of the original and extracted signal is comparable.
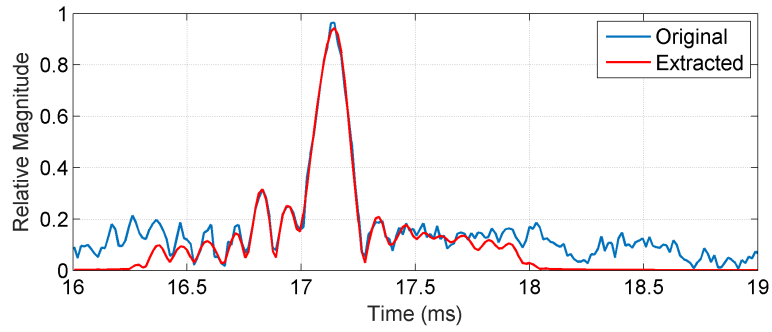
Effective separation of both main and tail rotor blades can be achieved for this data set using
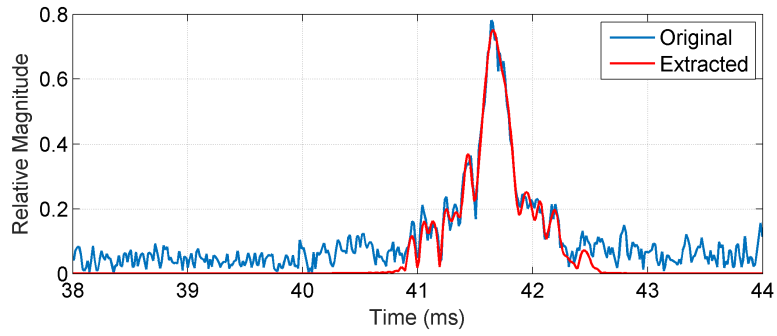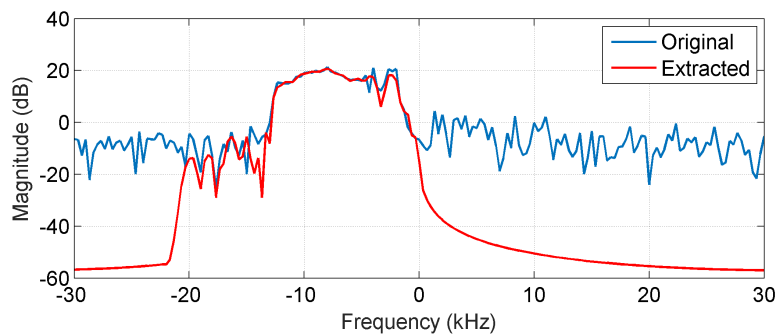
(a) Time-domain signals of the first approaching main blade
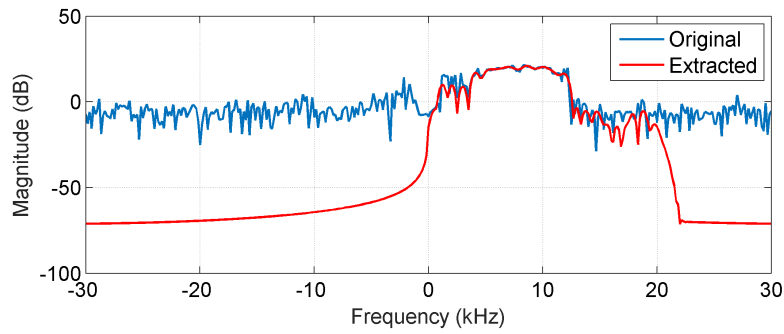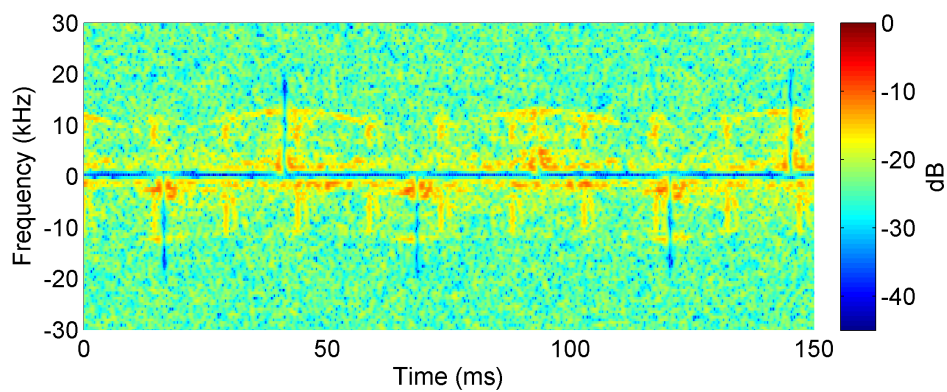

(b) The same signals as above, in frequency domain

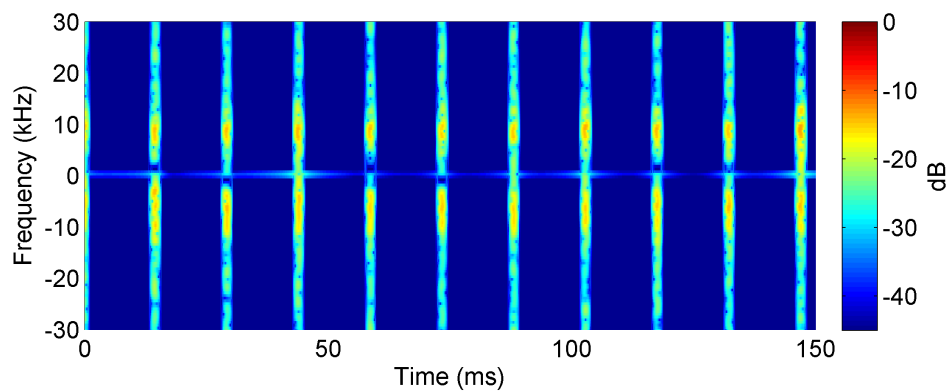(c) Time-domain signals of the first receding main blade

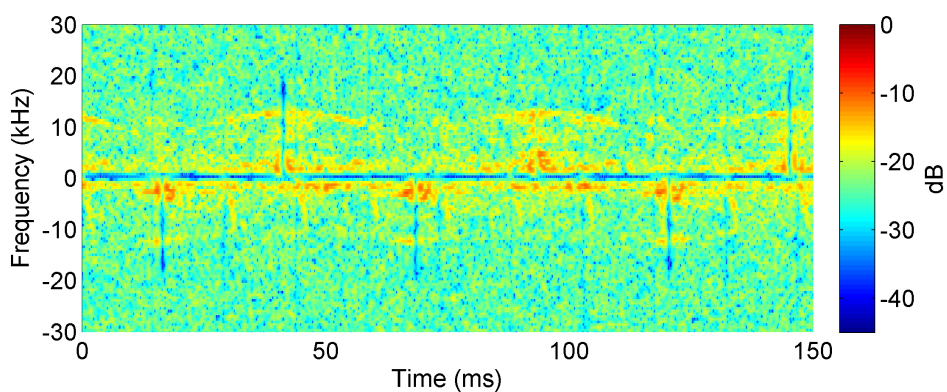(d) The same signals as in (c), in frequency domain

Figure 22: Comparison of the original and extracted signals for the first main rotor blade, at X-band, 45° aspect, Squirrel helicopter data.

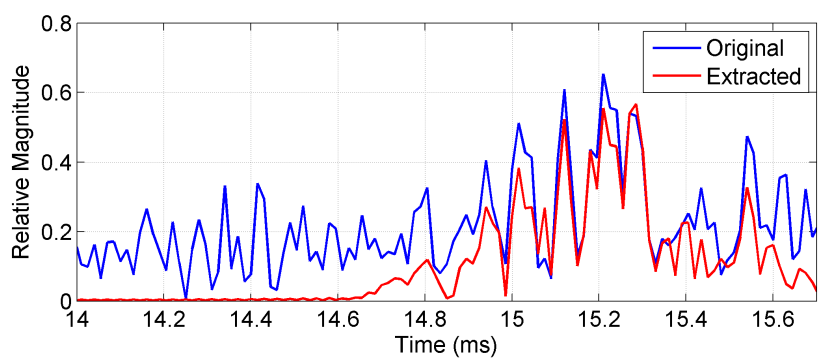(a) Signal after the main rotor blade extraction
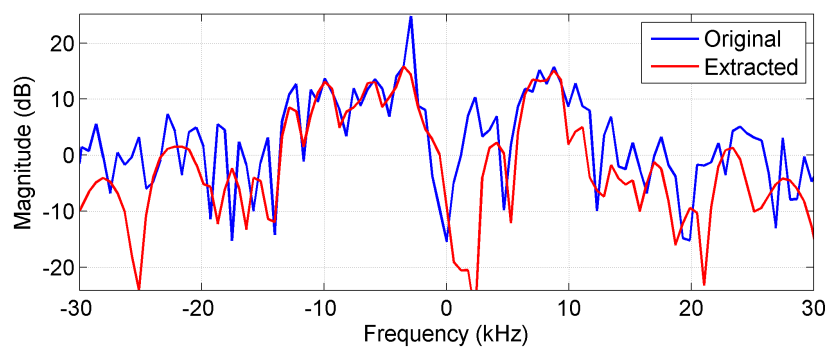

(b) Spectrogram of the extracted tail rotor components

(c) The residual signal after the tail rotor extraction

Figure 23: Stage 3 processing – for the tail rotor blades – on Squirrel helicopter data, at X-band, 45° aspect.

(a) Time-domain signals of the first tail rotor blade flash

(b) The same signals as above, in frequency domain

Figure 24: Comparison of the original and extracted signals for the first tail rotor blade, at X-band, 45° aspect, Squirrel helicopter data.

the same parameters used for simulated data discussed in Section 3.2.

4.2   Experimental data at X-band: $180°$ aspect

Consider the data set with operating frequency at X-band and aspect angle of $180°$. The difference in aspect angle results in radar returns having different intensity components as compared to the previous data set, especially in the tail rotor component, reflected in the spectrogram in Figure 25(a).

The magnitude of the tail component is significantly different compared to that of the $45°$ aspect angle (see Figure 20(b)) as the approaching tail component is now more dominant compared to the receding one. Applying Stage 2 processing for main rotor extraction, and using the parameters, $Q = 6, r = 25, J = 40$, the separated main rotor and the residual signals are shown in Figure 25. Even in the presence of more dominant tail rotor returns, the main blade extraction is effective.

The time domain and Doppler plots of the first approaching and receding main blades of the original and extracted signals are shown in Figure 26. Effective extraction of the main blades can be obtained for this data set using the same parameters used previously.

As before, the signal after main blade extraction is used as the input to Stage 3, tail blade processing, using TQWT parameters $Q = 1.2, r = 20, J = 17$. The full tail blades energy is correctly extracted after Stage 3.2 processing, noting that for this data set the approaching tail blade (positive Doppler) has a stronger magnitude than the receding one (negative Doppler). This is captured in Figure 27(b) which shows the spectrogram of the extracted tail blade component. Figure 27(c) shows the spectrogram of the residual signal.

The signal from the first tail rotor blade is plotted in the time and frequency domains, in Figure 28(a) showing the comparison between the original and extracted tail blade signal in the time-domain. Again, the two signals are comparable with temporal features extracted correctly, but with some variation in magnitude. Figure 28(b) shows the comparison between the original and extracted tail blade signal in the frequency-domain.

Since the same TQWT parameters were used for all X-band data sets (simulated, $45°$ and $180°$ aspects), signal separation for both main and tail blades was achievable using the same wavelet parameters Q, r, J, θ. This suggests that provided the same operational frequency and PRF is being used, which ensures the Doppler and temporal characteristic don't change, the algorithm is not sensitive to changes in aspect angle.
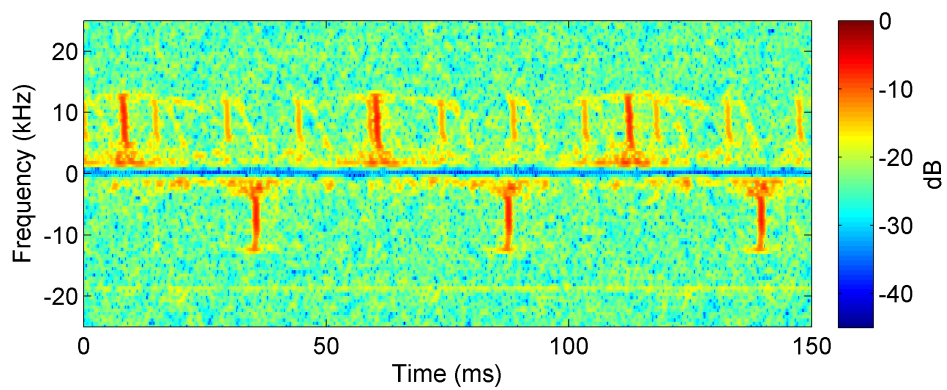
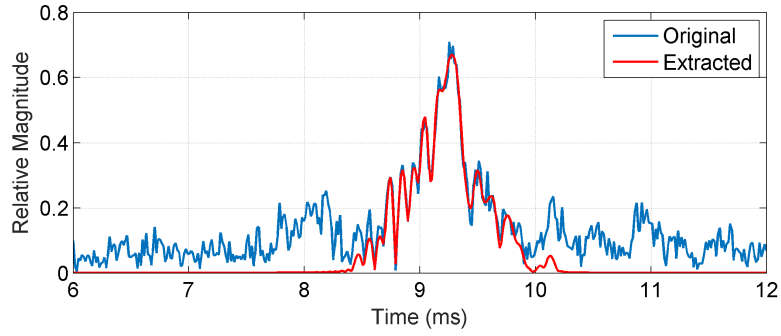(a) The pre-processed signal as input to Stage 2 processing
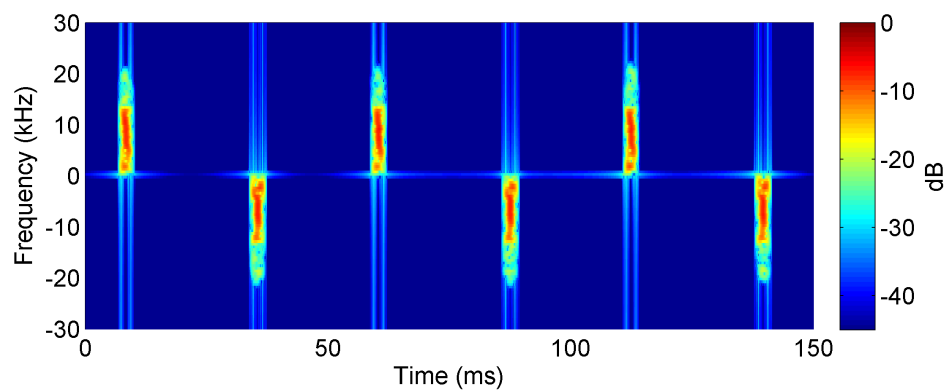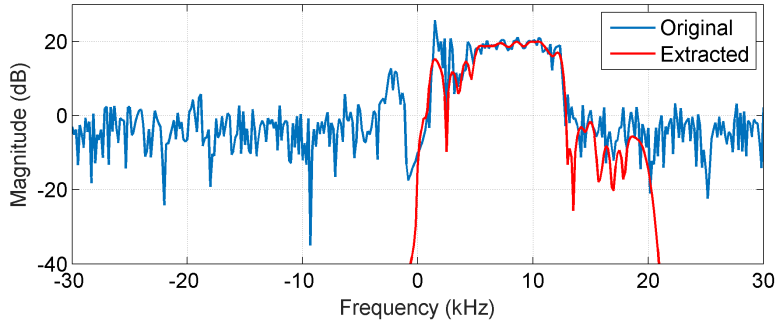

(b) The extracted main blade components
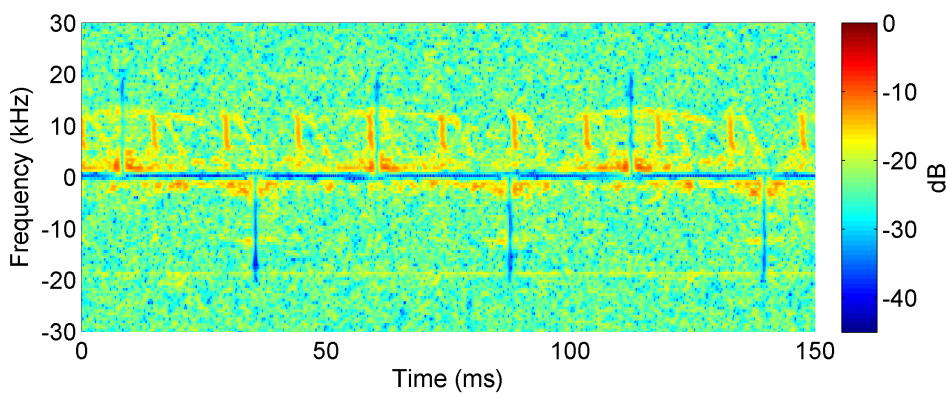
(c) The residual signal

Figure 25: Stage 2 processing – for the main rotor blades – on Squirrel helicopter data, at X-band, 180° aspect.
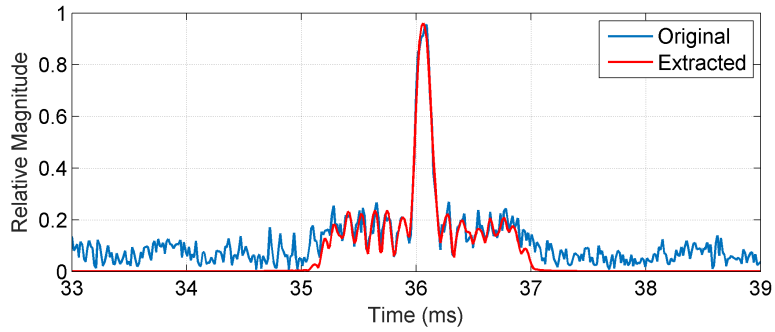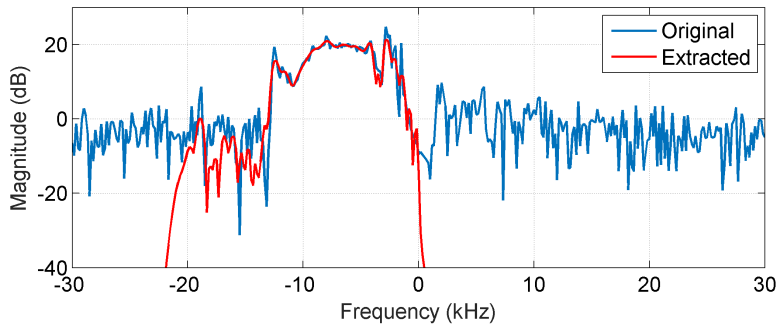
(a) Time-domain signals of the first approaching main blade

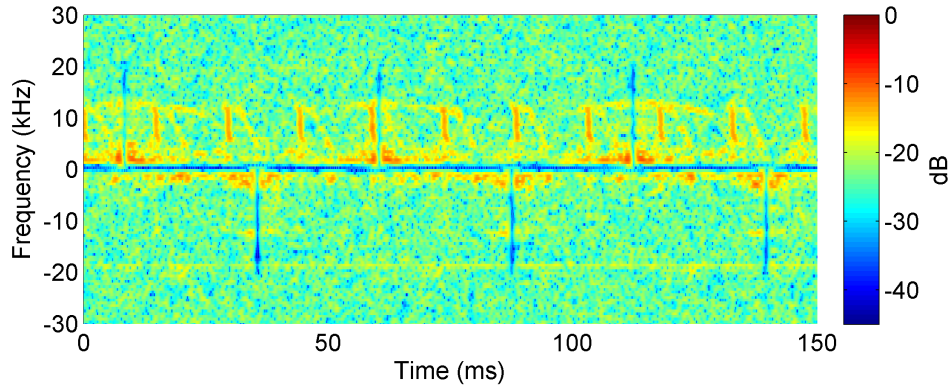(b) The same signals as in (a), in frequency domain

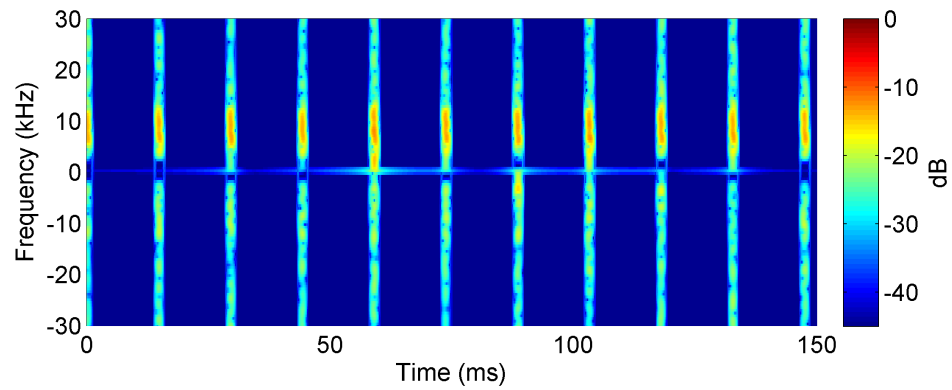(c) Time-domain signals of the first receding main blade

(d) The same signals as in (c), in frequency domain

Figure 26: Comparison of the original and extracted signals for the first main rotor blade, at X-band, 180° aspect.
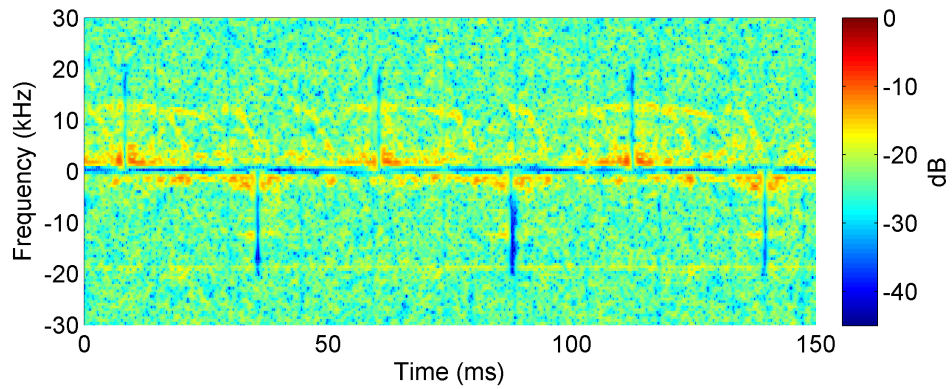
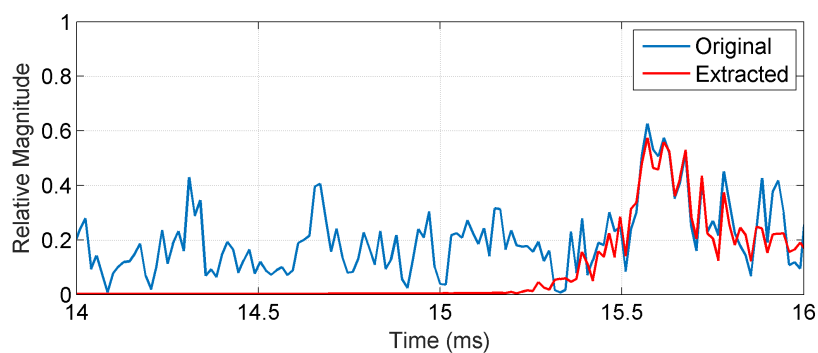(a) The input signal after main blade extraction

(b) The extracted tail blade components
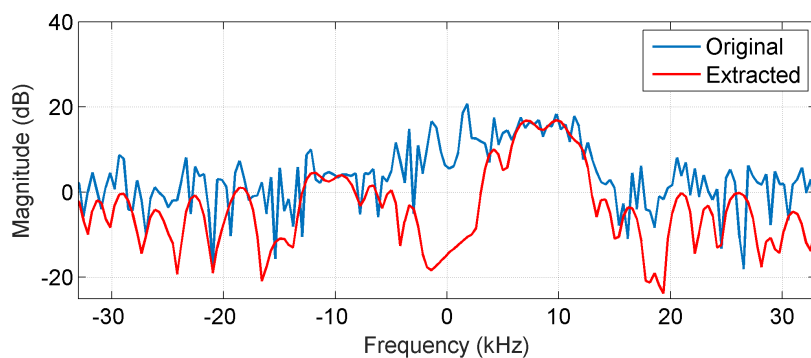

(c) The residual signal after tail blade extraction

Figure 27: Stage 3 processing – for the tail rotor blades – on Squirrel helicopter data, at X-band, 180° aspect.

(a) Time-domain signal of the first tail blade flash

(b) The same signal as bove, in frequency domain

*Figure 28:   Comparison of the original and extracted signals for the first tail rotor blade, 180°
aspect.*

4.3   Experimental data at Ku-band: nose aspect

In this section we present results of the proposed technique applied to Ku-band radar data (16.8 GHz) measured at an aspect angle of 0°. At this higher operational frequency (shorter wavelength), finer details of the rotor blade are observed resulting in stronger specular returns, due to the nature of the backscattering phenomena. Furthermore, broadening in both time and frequency-domains for the main and tail rotor blades has changed significantly compared to the X-band data.

The spectrogram of the Ku-band data after Stage 1 preprocessing is shown in Figure 29(a). The Doppler spread of the main rotor component extends to approximately 25 kHz compared to 15 kHz for the X-band data[4]. Also, the reflectivity of the tail blade flash is not constant for all frequencies, with a large return from approximately 10 kHz to 15 kHz but reducing in strength beyond this frequency.

The same TQWT and algorithm parameters as used for the X-band data are applied to this DC filtered signal. The main blades separation after Stage 2.2 processing is shown in Figure 29(b). The blade is successfully extracted in both time and frequency, with the residual signal spectrogram shown in Figure 29(c).

Figure 30(a) shows a comparison between the original and extracted time-domain signals of the first approaching main blade, after Stage 2.2 processing for this Ku-band data. The results show very good correlation between the original and extracted signal in both the shape, magnitude of the responses and side-lobe structure. This plot also shows that the large flash response at times $18.3 - 18.4$ ms has a shorter duration in time, compared to the X-band data, but the flash response over the period of $17 - 19.5$ ms is still captured, giving good extraction of the blade flash signal. The frequency response of this first approaching blade flash signal is shown in Figure 30(b). Similarly, the correlation between the original and extracted signal is very good, with the Doppler extent and response shape of the extracted signal matching the original signal very closely.

The time-domain plot of the first receding main blade is shown in Figure 30(c). The plot highlights how well the processing works on this signal in extracting the main blade response. Figure 30(d) illustrates the broad and fluctuating Doppler response over the frequency range -25 to 0 kHz, which is representative of main blade returns at high operational frequencies. This can potentially be an issue for weaker returns since the algorithm may not treat the blade as one broad-band component but instead treating them as various components; for example, one broad-band from -25 to -10 kHz and two separate narrow-band components at -5 kHz and -2 kHz.

As was shown for the X-band data, the technique is applied to extract the tail rotor blade return from the residual signal after the main rotor blades extraction. The spectrogram with the tail blade component only is re-shown in Figure 31(a) for a visual reference. The tail component can be observed on both sides of the frequency spectrum, but the receding blade (negative Doppler frequencies) produces a much greater response. In fact, the approaching tail rotor blade response is comparable to the background noise and is only slightly discernible to the observer.
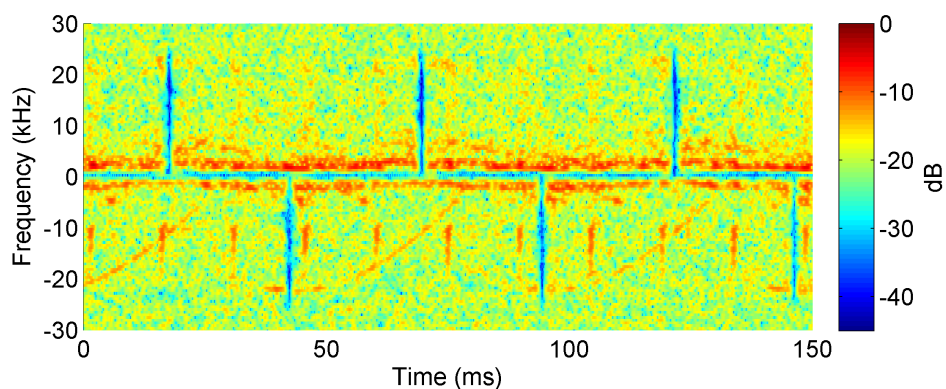
---

[4]Note that main rotor Doppler extent ratio (25kHz/15kHz) more or less matches the ratio of frequencies (16.8GHz/9.5GHz)
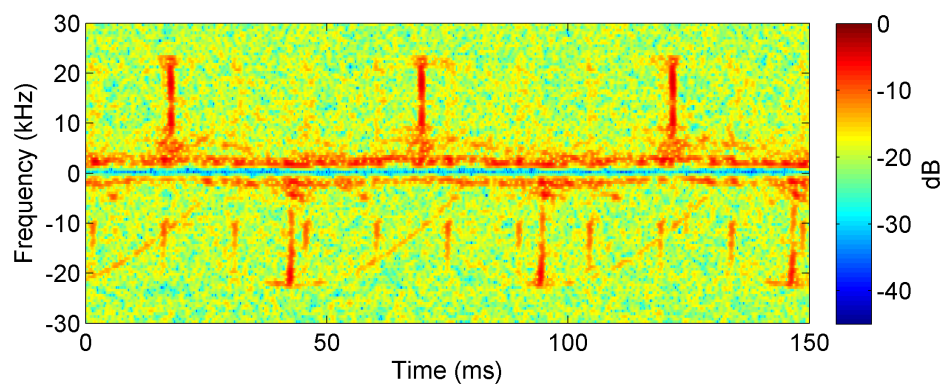
(a) The pre-processed signal
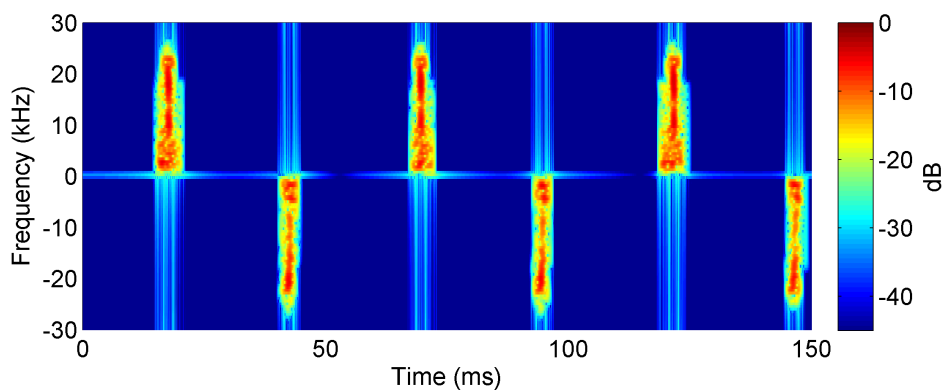
(b) The extracted main blade components

(c) The residual signal

Figure 29:   Results of Stage 2 processing on Squirrel helicopter data, at Ku-band, nose aspect.

As before, the same TQWT and algorithm parameters as used for the X-band data are applied to the tail only signal. Figure 31(b) shows the extracted signal after Stage 3.2 processing and Figure 31(c) shows the residual signal.

The effectiveness of the tail extraction is more clearly seen in Figure 32 where the first tail rotor blade is plotted in the time and frequency domains. Figure 32(a) shows the comparison between the original and extracted tail blade signal in the time-domain. Figure 32(b) shows the comparison between the original and extracted tail blade signal in the frequency-domain. In both cases, the shape and magnitude of the original and extracted signal are comparable.

Although the extraction of the main and tail rotor is successfully demonstrated at Ku-band, more work for this operational frequency (and potentially lower frequencies) is needed, where scattering phenomena plays a more significant role in the time and frequency responses, which determines the optimal parameters and transform domains for this problem.
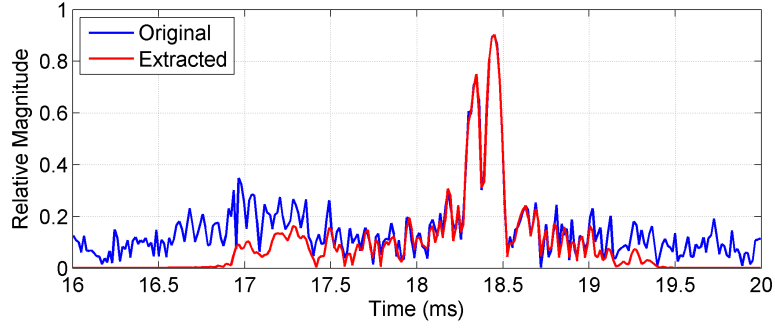
(a) Time-domain signals of the first approaching main blade
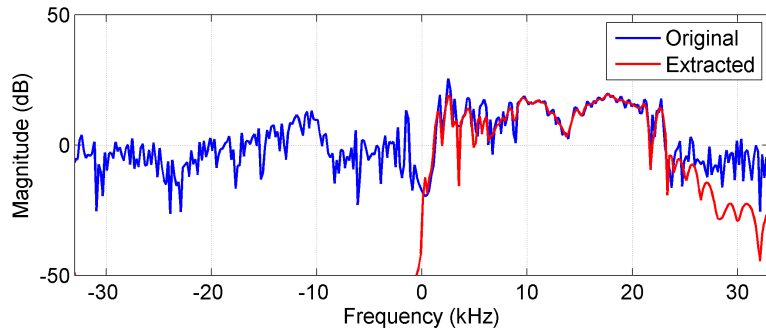
(b) The same signals as in (a), in frequency domain
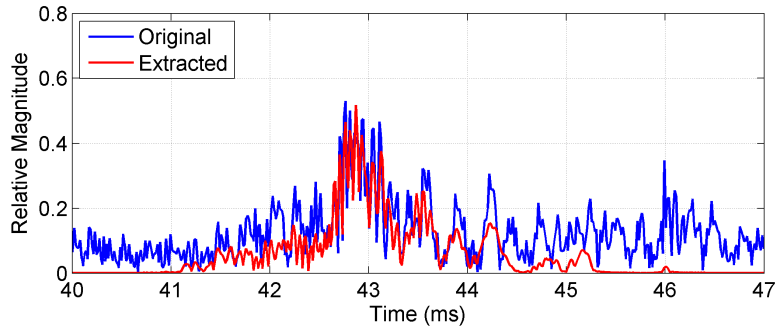
(c) Time-domain signals of the first receding main blade
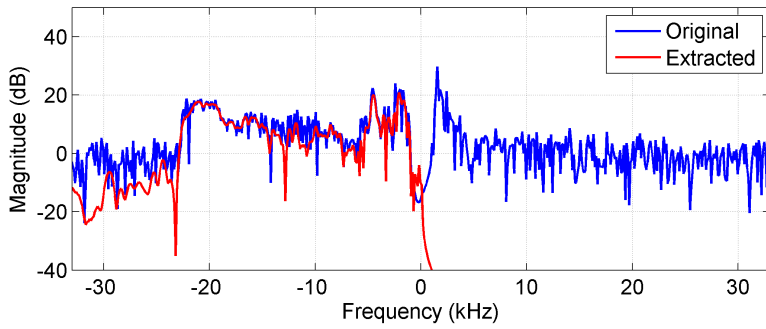
(d) The same signals as in (c), in frequency domain

Figure 30:   Signal comparison for the first approaching and receding main blade, at Ku-band

(a) Spectrogram after main blade extraction

(b) Extracted tail signal

(c) Residual signal
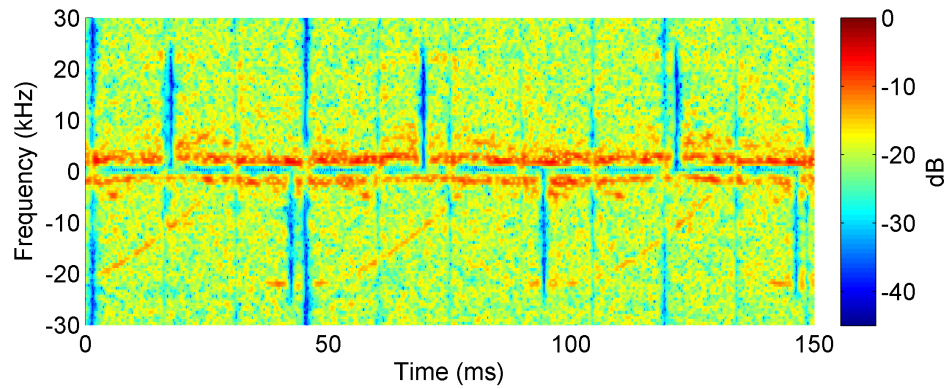
Figure 31: Results of Stage 3 processing on Squirrel helicopter data, at Ku-band

(a) Time-domain signals of the first tail blade flash

(b) The same signals in (a), in frequency domain

Figure 32: Comparison of signals in Stage 3 processing of the first tail blade flash signal at Ku-band.
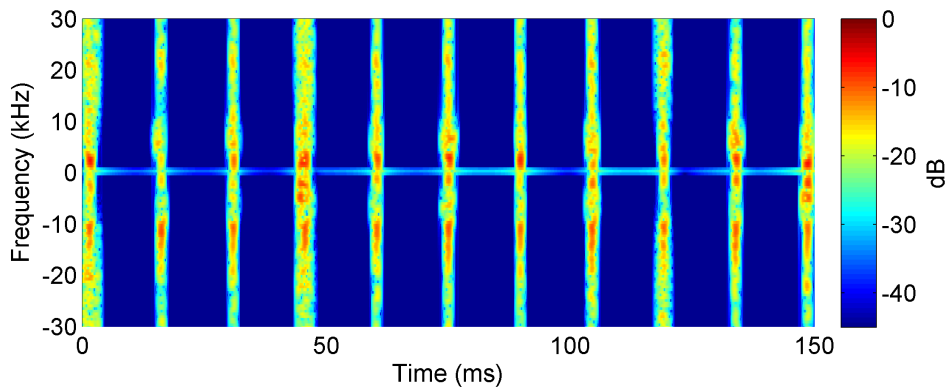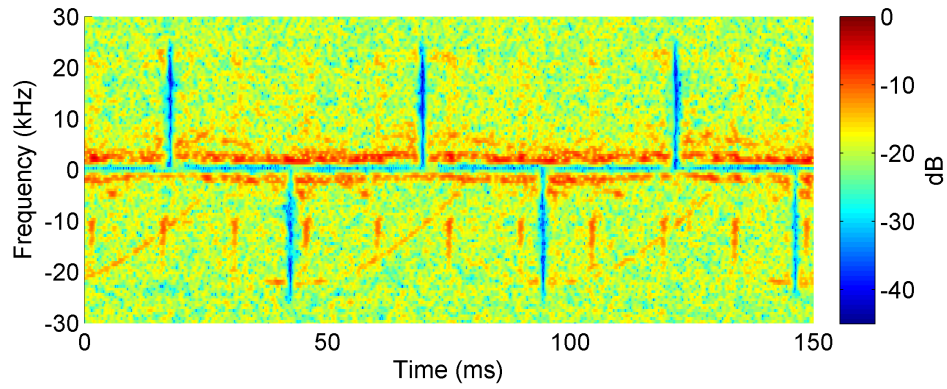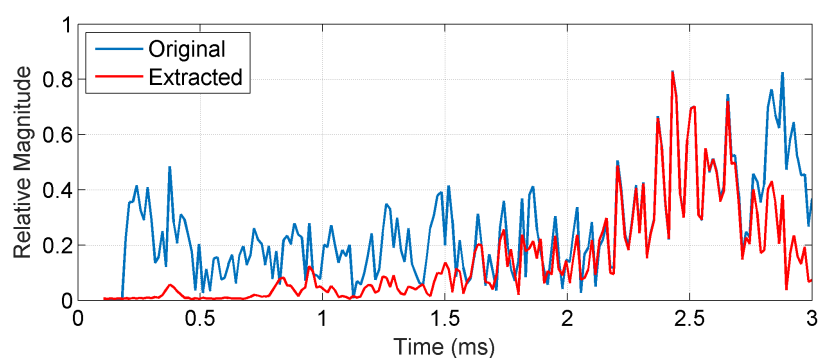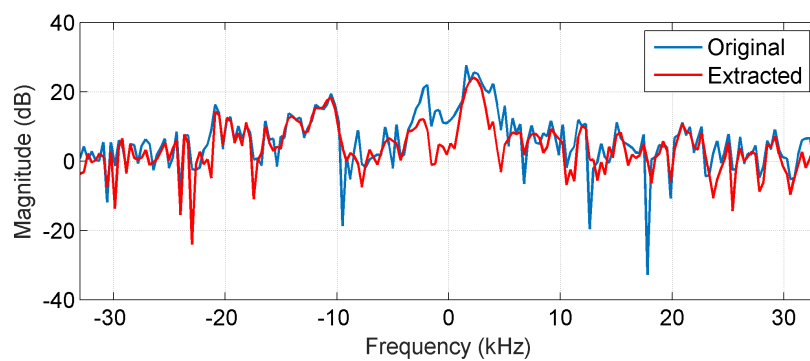
5 Signal separation with sea clutter interference

This section discusses the extraction of the main rotor blades in the presence of sea clutter. In many practical scenarios of interest the radar may operate in the environments where sea clutter is present, thus the proposed algorithm needs to be robust to such clutter interference.

Simulated sea clutter at sea state 2 using the GIT clutter model [45] is generated using the Generic Phased Array Radar Model (GPARM) version 2015a developed by the DST Group for similar radar and waveform parameters as in the X-band real data: carrier frequency of 9.5 GHz, 1μs long rectangular pulses without waveform coding, PRF of 67.1 kHz, 64 pulse CPIs, and 0.1μs sampling intervals. Clutter data in a single representative range bin was used for analysis.

The simulated sea clutter is then added to the real X-band data with aspect angle of 45 degrees, which was described in Section 4, at various signal to clutter ratio (SCR) levels. If the real data is denoted as $\boldsymbol{x}_{signal}$ and the simulated sea clutter data as $\boldsymbol{x}_{clutter}$, the additive signal is given by

$$\boldsymbol{y} = \boldsymbol{x}_{signal} + \boldsymbol{x}_{clutter}, \tag{11}$$

and is used to test the proposed algorithms at two different SCR levels, where

$$SCR_{total} = 10 \log_{10} \frac{\sum_n |\boldsymbol{x}_{signal}[n]|^2}{\sum_n |\boldsymbol{x}_{clutter}[n]|^2} \quad \text{(dB)}.$$

The total signal to clutter ratio defined here is computed for the composite signal of the helicopter which includes all components: the helicopter body, the hub, and the blades. Since the signal of interest is only the main blades component, we also use an SCR defined only for the main blades, called 'main blades SCR', SCR_{MB}, as

$$SCR_{MB} = 10 \log_{10} \frac{\sum_n |\hat{\boldsymbol{x}}_{MB}[n]|^2}{\sum_n |\boldsymbol{x}_{clutter}[n]|^2},$$

where $\hat{\boldsymbol{x}}_{MB}$ is computed (i.e. estimated) using the extracted main blades signal after the separation algorithm is applied.

The strong returns of the sea clutter are concentrated around the low Doppler frequencies with some leakage to higher frequencies depending on the SCR level. Lower SCR means stronger sea clutter energy and stronger leakage energy to higher Doppler frequencies. Hence, the problem can be treated in a manner similar to that of tail rotor extraction with strong interference relative to the signal components of interest in the low Doppler frequency region (Stage 3 processing). To accommodate various levels of SCR, the father wavelet was designed to have a frequency range from -6.5 to 6.5 kHz, and the TQWT parameters are set to $Q = 1.5, r = 10, J = 12$.

In the first experiment, the total SCR is set to 10 dB. The original signal and sea clutter contaminated signal are shown in Figure 33(a) and Figure 33(b), respectively. After Stage 1 processing, the pre-processed signal is shown in Figure 34(a). The extracted main blades component is shown in Figure 34(b), and the residual signal is shown in Figure 34(c). The

main blades components have been successfully extracted from clutter and all the clutter components remain in the residual signal.

The time-domain and associated frequency-domain plots of the extracted first receding and approaching blades are shown in Figure 35. From the time-domain plots it is clear that the algorithm is capable of correctly extracting the main blade components. Here, the main blades SCR was estimated to be -4.4 dB.

(a) Original helicopter data

(b) Original data with additive clutter at $SCR_{total} = 10$ dB

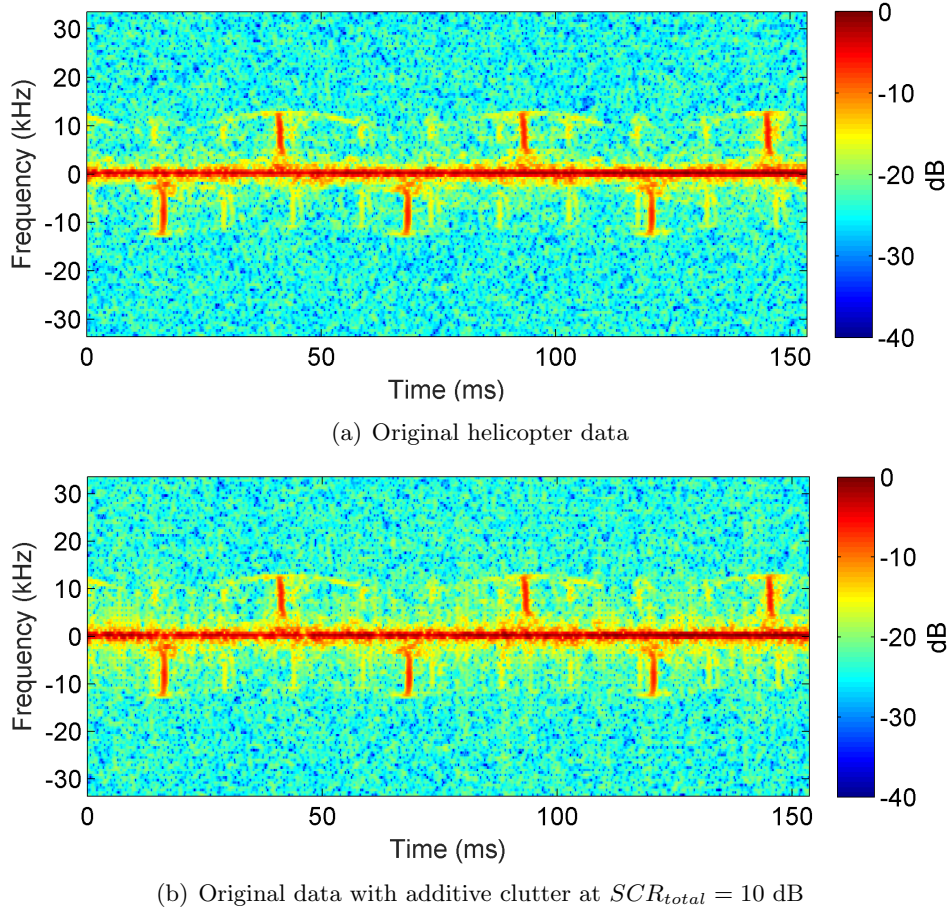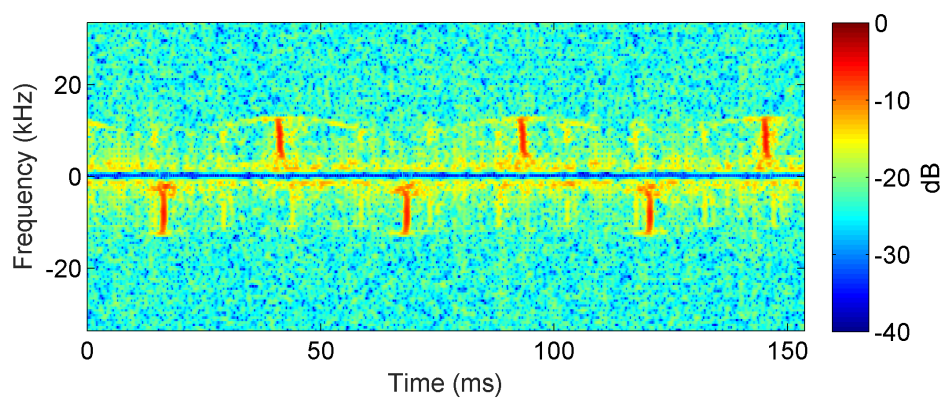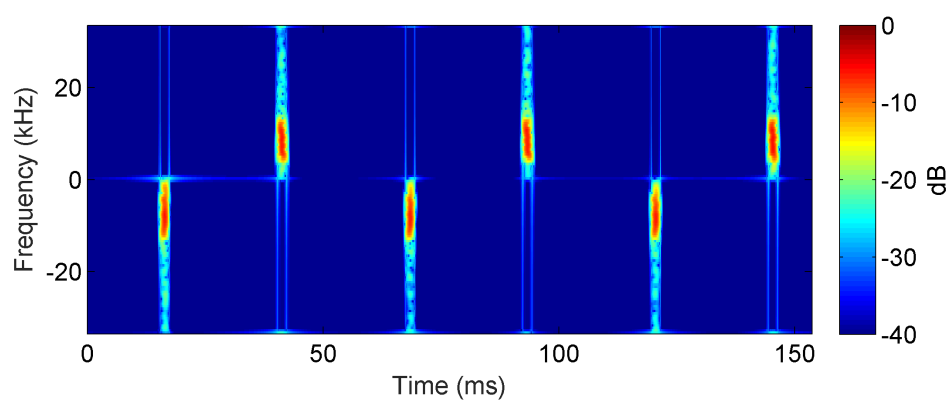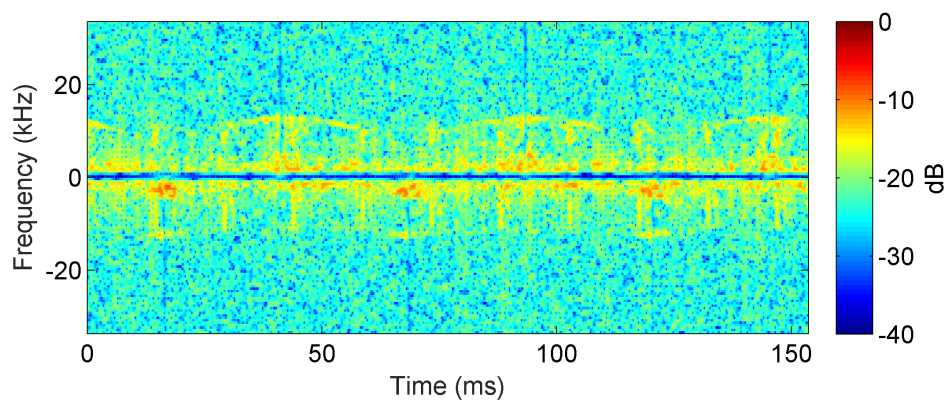*Figure 33: Data with and without simulated clutter, at X-band, 45° aspect, $SCR_{total} = 10$ dB.*

(a) The pre-processed signal

(b) The extracted main blade signal

(c) The residual signal

Figure 34: Stage 2 processing of sea clutter contaminated data, at X-band, 45° aspect and $SCR_{total} = 10$ dB.

DST-Group–RR–0436

Now, we repeat the above analysis with total SCR set to -11.7 dB. This is the minimum SCR required for the algorithm to effectively extract the main blade components. The spectrograms of the clutter contaminated signal and the extracted main blade component are shown in Figures 36(a) and 36(b), respectively. When the total SCR is -11.7 dB, there are significant clutter transients and the main blade components are hardly distinguishable from the sea clutter components, illustrated in Figure 36(a). In spite of this, the proposed algorithm is capable of recovering the main blade signal from the strong clutter background as shown in Figure 36(b). This shows the robustness of the method even at low signal levels.

The first approaching and receding main blades signals are shown in Figure 37 in time and frequency domains. Even though, the clutter transients have larger magnitude than the main blade signal, as shown in the time-domain plots, the proposed method correctly identifies and extracts the signal of interest, and the extracted signal is very similar to the original clutter-free signal. Also, clutter peaks closely overlap with the main blade returns as can be seen from Figures 37(a) and 37(c). Note that strong clutter returns are present within 0.5 ms of blade returns. The proposed technique can still extract the blade signals without extracting the clutter components. A simple time domain method where a time window around the blade flash is used, assuming time occurrence of the blade flash can be correctly identified, to extract the blade signal will not work, as such an extraction will certainly be contaminated by the clutter returns.

The total SCR of -11.7 dB is the smallest signal to clutter ratio where the proposed approach can still be effective for main rotor blades separation, corresponding to a main blades SCR of -25 dB (when only main blade signal is considered). The ability of the algorithm to extract components of interest at such a low SCR is promising and demonstrates the robustness of the method. However, the GIT clutter model used to generate simulated clutter data does not emulate clutter Doppler spectrum due to correlation, thus more experiments with real clutter data should be done for verification.

We also compare the extracted blade signals in clutter environment with the same extracted signals from section 4 where no clutter was present. The comparison results are shown in Figure . Main blade extraction in clutter was done at SC of -11.7 dB. The extracted signals with and without clutter are a close match to each other demonstrating the robustness of the proposed technique to significant clutter levels.

The tail rotor blade extraction in clutter depends on the aspect angle of the helicopter target. It was found that a minimum total SCR of 10 dB is required for effective tail blades separation using the same parameters of Q, R, J, θ as for the clutter free scenario. The 'tail blades SCR' of tail rotor blades to clutter in this case is -17 dB. Again, this minimum SCR is highly dependent on the target aspect to the radar.
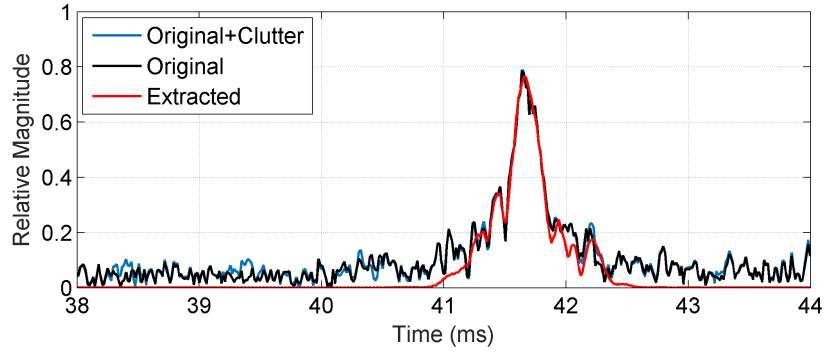
(a) Time-domain signals of the first approaching main blade
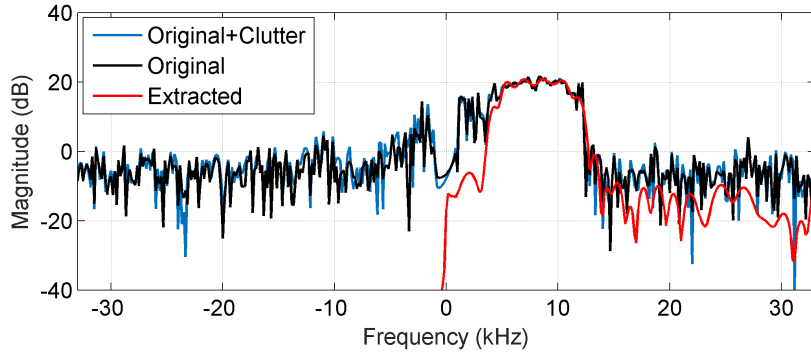
(b) The same signals as in (a), in frequency domain
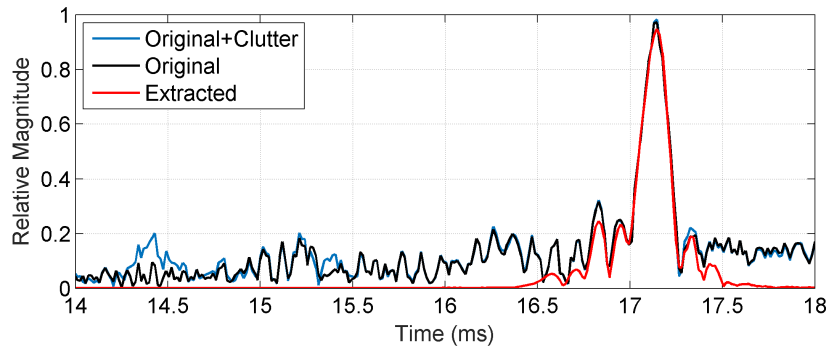
(c) Time-domain signals of the first receding main blade
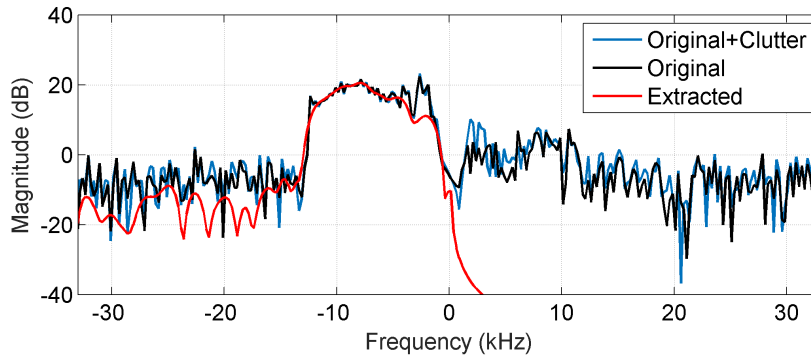
(d) The same signals as in (c), frequency domain

Figure 35: Comparison of signals for the first main blade, $SCR_{total} = 10$ dB at X-band and 45° aspect.

(a) The pre-processed signal
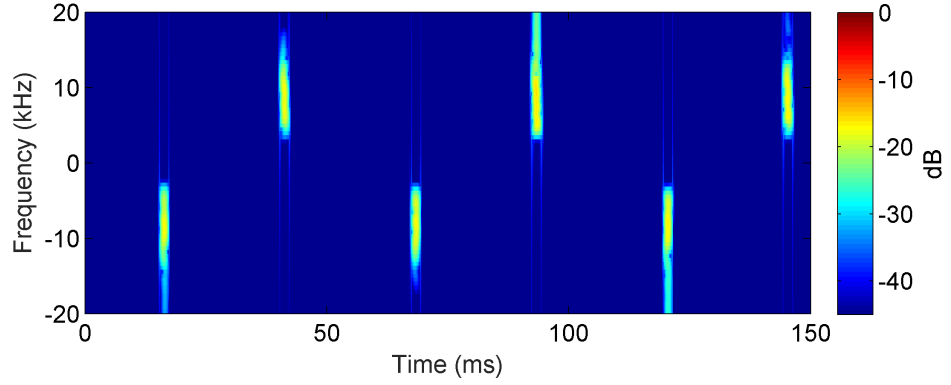
(b) The extracted main blade signal
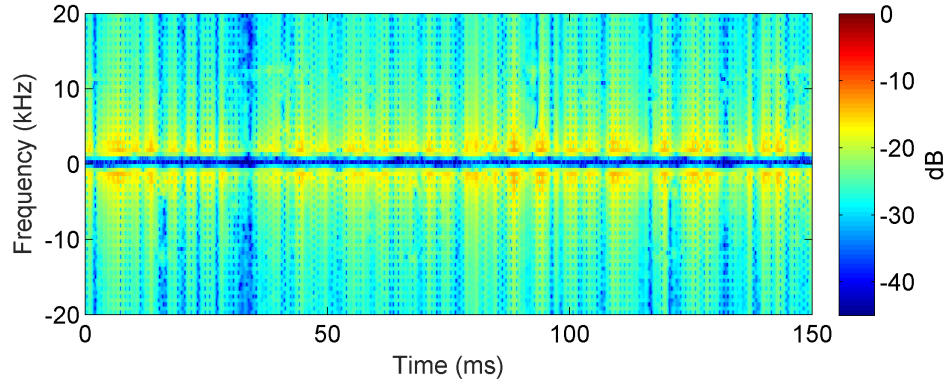
(c) The residual signal

Figure 36: Stage 2 processing, X-band, 45° aspect, $SCR_{total} = -11.7$ dB.
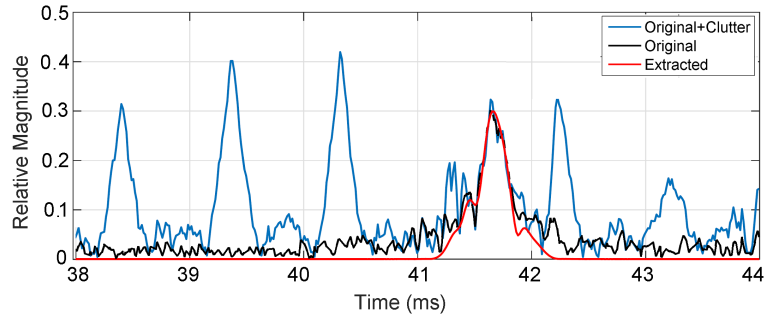
(a) Time-domain signals of the first approaching main blade
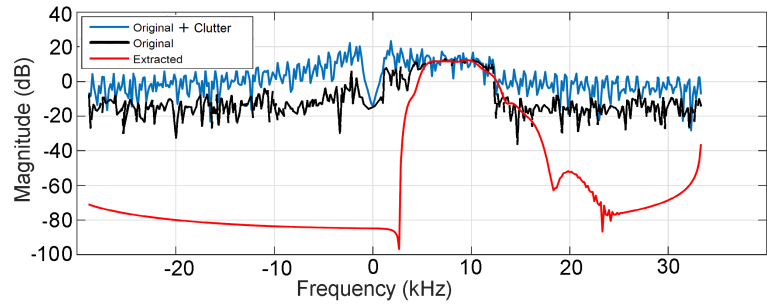
(b) The same signals in (a), in frequency domain

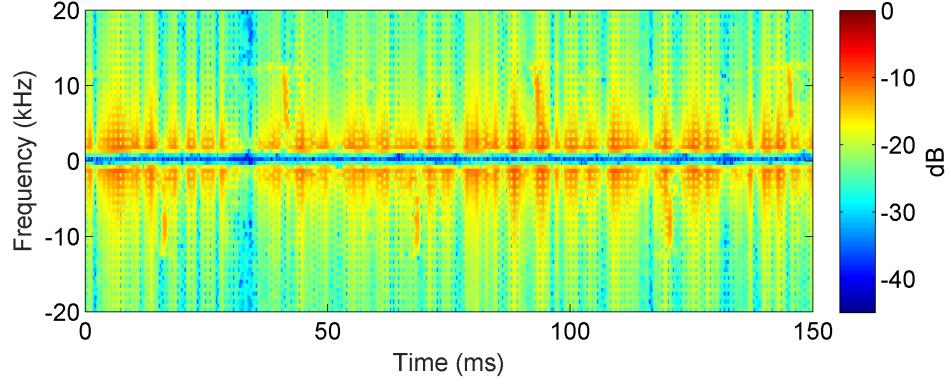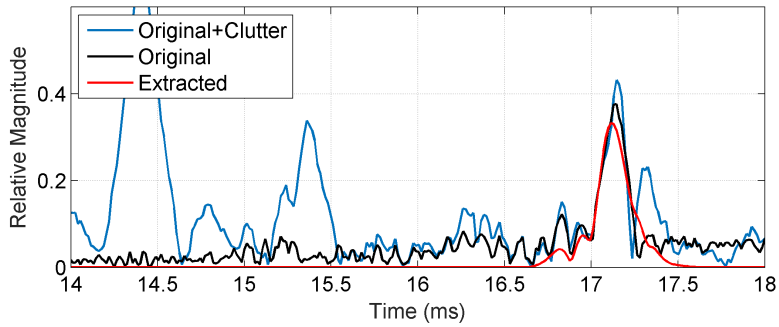(c) Time-domain signals of the first receding main blade
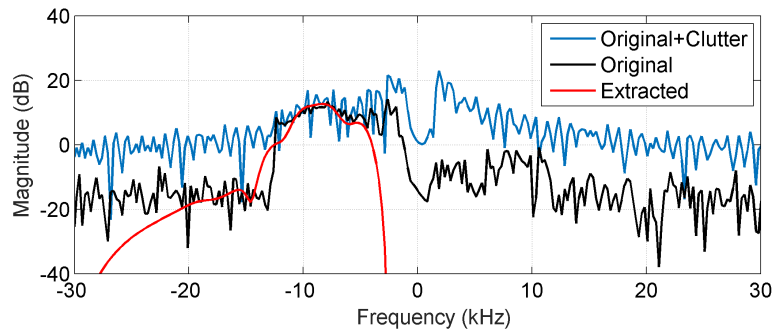
(d) The same signals as in (c), frequency domain

Figure 37: Comparison of signals in Stage 2, with $SCR_{total} = -11.7$ dB, at X-band and 45° aspect.
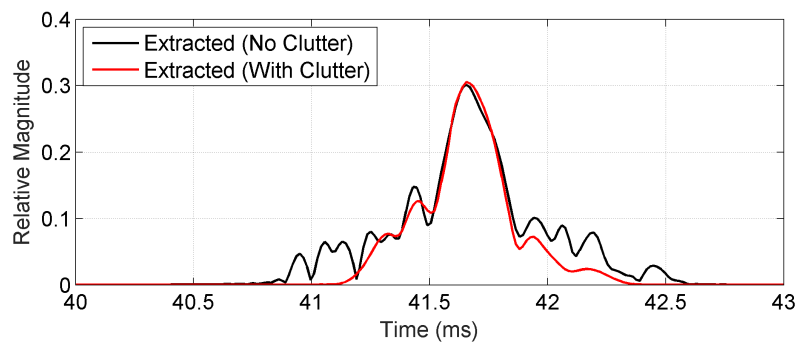
(a) First approaching main blade
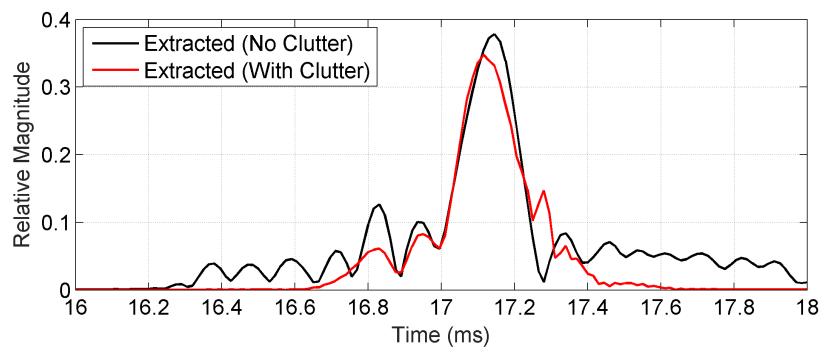
(b) First receding main blade

Figure 38: Comparison of extracted blade signal with and without simulated clutter added for approaching and receding main blades.

6   Remarks and Discussion

The selection of Q, r, J parameters for TQWT construction is critical for the proposed algorithm in obtaining a sparse solution. The optimal set of parameters will depend on the physical properties of the blades such as length and rotational speed, as well as radar and waveform parameters such as operational frequency and PRF. Currently, parameters are tuned with this prior knowledge for a given data set. Future work is warranted to develop an automated search algorithm for estimating a good set of values for these parameters using Doppler and temporal characteristics of initial blade flashes as training data.

For a long CPI as in the application of interest, the computation of the linear and inverse transforms of the input vector $\boldsymbol{x}$ will be a dominant factor. As discussed, the forward and the inverse transform matrices $\boldsymbol{\Phi}$ and $\boldsymbol{\Psi}$ are not explicitly constructed in the algorithm, thus saving a great amount of storage and computation. The linear and inverse transforms are implemented by an iterative filter bank operation, discussed in section 2.1.1. For an input signal $\boldsymbol{x}$ of N samples, the computational cost of TQWT is $O(rN \log_2 N)$ as discussed in [38]. The BPD problem is solved using the SALSA algorithm as stated in algorithm 1, which requires P iterations to converge (the algorithm usually converges within 50 iterations), each of which involves one forward and one inverse TQWT. Hence, the computational cost of the proposed algorithm is in the order of $O(PrN \log_2 N)$.

The proposed signal separation algorithm was run on an Intel (R) Core i7 at 3.6 GHz with 8 GB memory for 150 ms CPIs, and the measured processing time was approximately 29 seconds for the parameters $Q = 6, r = 25, J = 40$. When compared to the existing work, which uses orthogonal matching pursuit (OMP) for the same problem as discussed in [46], the proposed method requires only 40 atoms to construct the dictionary compared to over 1000 atoms in the OMP approach. Also, it should be noted that in the OMP the search dictionary needs to be explicitly constructed.

In this report, the proposed signal separation algorithms were tested on X-band and Ku-band radar returns. The algorithms can be equally applicable to lower operational frequencies such as L-band, though further testing with radar data at those frequencies is warranted. Since the proposed algorithm exploits the differences in Doppler and temporal characteristics of different signal components, the algorithm may need to be tuned differently to take into account those characteristics for helicopter returns at low frequencies. More resolution in Doppler (high PRF and long CPIs) may be required to capture tail blade returns at low operating frequencies.

7   Conclusion

In this report, algorithms for effective separation into the main and tail rotor blades of the complex helicopter radar returns are demonstrated. The algorithms are based on the methods of sparse signal optimisation with the tunable Q wavelet transform, exploiting the inherent differences in the temporal and Doppler characteristics of the signal components of interest. The demonstration used both simulated and real data at X and Ku-bands.

Promising performance of the novel algorithms has been shown for a hovering Squirrel he-

DST-Group–RR–0436

licopter, with no significant translational motion and maneuvering and under clutter-free conditions. Partial results have been achieved under a simulated sea clutter environment; effective main blades separation at a signal to clutter ratio as low as -25 dB. A similar demonstration of the algorithms under real clutter and real target maneuvering remains to be done.

The proposed algorithms are found to be very effective for signal separation with relatively fast computation times thanks to the nature of implementation of the algorithm, particularly in solving the basis pursuit denoising problem, and in the computation of the forward and inverse wavelet transforms without matrix inversion. However, some parameter tuning was required using prior knowledge of the Doppler extent of the component of interest during the pre-processing stage. Future work is currently planned to automate the parameter tuning step.

Acknowledgements

8   References

[1] Chen, V. C. (2000) Analysis of radar micro-Doppler with time-frequency transform, *in Proceedings of the 10th IEEE Workshop on Statistical Signal and Array Processing*, pp. 463–466.

[2] Chen, V. C., Li, F., Ho, S. & Wechsler, H. (2006) Micro-Doppler effect in radar: phenomenon, model, and simulation study, *IEEE Transactions on Aerospace and Electronic Systems* **42**(1), 2–21.

[3] Chen, V. C. (2011) *The micro-Doppler effect in radar*, Artech House.

[4] Chen, V., Li, F., Ho, S.-S. & Wechsler, H. (2003) Analysis of micro-Doppler signatures, *IEE Proceedings - Radar, Sonar and Navigation* **150**(4), 271–276.

[5] Stankovic, L., Djurovic, I. & Thayaparan, T. (2006) Separation of target rigid body and micro-Doppler effects in ISAR imaging, *IEEE Transactions on Aerospace and Electronic Systems* **42**(4), 1496–1506.

[6] Stankovic, L., Thayaparan, T., Dakovic, M. & Popovic-Bugarin, V. (2013) Micro-Doppler removal in the radar imaging analysis, *IEEE Transactions on Aerospace and Electronic Systems* **49**(2), 1234–1250.

[7] Yilmaz, O. & Rickard, S. (2004) Blind separation of speech mixtures via time-frequency masking, *Signal Processing, IEEE transactions on* **52**(7), 1830–1847.

[8] Feng, Z., Liang, M. & Chu, F. (2013) Recent advances in time–frequency analysis methods for machinery fault diagnosis: a review with application examples, *Mechanical Systems and Signal Processing* **38**(1), 165–205.

[9] Chen, V. C. & Ling, H. (2001) *Time-frequency transforms for radar imaging and signal analysis*, Artech House.

[10] Qian, S. & Chen, D. (1993) Discrete Gabor transform, *IEEE Transactions on Signal Processing* **41**(7), 2429–2438.

[11] Daubechies, I. (1990) The wavelet transform, time-frequency localization and signal analysis, *IEEE Transactions on Information Theory* **36**(5), 961–1005.

[12] Li, P., Wang, D.-C. & Wang, L. (2013) Separation of micro-Doppler signals based on time frequency filter and Viterbi algorithm, *Signal, Image and Video Processing* **7**(3), 593–605.

[13] Suresh, P., Thayaparan, T., Obulesu, T. & Venkataramaniah, K. (2014) Extracting micro-Doppler radar signatures from rotating targets using Fourier–Bessel transform and time–frequency analysis, *IEEE Transactions on Geoscience and Remote Sensing* **52**(6), 3204–3210.

[14] Li, J. & Ling, H. (2003) Application of adaptive chirplet representation for ISAR feature extraction from targets with rotating parts, **150**(4), 284–291.

[15] Setlur, P., Amin, M. & Thayaparan, T. (2005) Micro-Doppler signal estimation for vibrating and rotating targets, *in Proceedings of the 8th International Symposium on Signal Processing and Its Applications*, pp. 639–642.

[16] Fulin, S. & Mingyuan, J. (2010) ISAR imaging of target with micro-motion parts based on SSA, *in 8th European Conference on Synthetic Aperture Radar (EUSAR)*, pp. 86–89.

[17] Clemente, C. & Soraghan, J. J. (2012) Vibrating micro-Doppler signature extraction from SAR data using singular value decomposition, *in 9th European Conference on Synthetic Aperture Radar (EUSAR)*, pp. 191–194.

[18] Chen, V. C. (2005) Spatial and temporal independent component analysis of micro-Doppler features, *in IEEE International Radar Conference*, pp. 348–353.

[19] Cai, C., Liu, W., Fu, J. S. & Lu, L. (2005) Empirical mode decomposition of micro-Doppler signature, *in IEEE International Radar Conference*, pp. 895–899.

[20] Bai, X., Xing, M., Zhou, F., Lu, G. & Bao, Z. (2008) Imaging of micromotion targets with rotating parts based on empirical-mode decomposition, *IEEE Transactions on Geoscience and Remote Sensing* **46**(11), 3514–3523.

[21] Cai, C., Liu, W., Fu, J. S. & Lu, Y. (2010) Radar micro-Doppler signature analysis with HHT, *IEEE Transactions on Aerospace and Electronic Systems* **2**(46), 929–938.

[22] Stankovic, L., Orovic, I., Stankovic, S. & Amin, M. (2013) Compressive sensing based separation of non-stationary and stationary signals overlapping in time-frequency, *IEEE Transactions on Signal Processing* **61**(18), 4562–4572.

[23] Orovic, I., Stankovic, S. & Stankovic, L. (2014) Compressive sensing based separation of LFM signals, *in 56th International Symposium ELMAR*.

[24] Hou, Q., Liu, Y. & Chen, Z. (2015) Reducing micro-Doppler effect in compressed sensing ISAR imaging for aircraft using limited pulses, *Electronics Letters* **51**(12), 937–939.

[25] Liu, Z., Wei, X. & Li, X. (2014) Aliasing-free micro-Doppler analysis based on short-time compressed sensing, *IET Signal Processing* **8**(2), 176–187.

[26] Stankovic, L., Stankovic, S., Thayaparan, T., Dakovic, M. & Orovic, I. (2015) Separation and reconstruction of the rigid body and micro-Doppler signal in ISAR Part I–Theory, *IET Radar, Sonar & Navigation,* **9**(9), 1147–1154.

[27] Stankovic, L., Stankovic, S., Thayaparan, T., Dakovic, M. & Orovic, I. (2015) Separation and reconstruction of the rigid body and micro-Doppler signal in ISAR part II–statistical analysis, *Radar, Sonar & Navigation, IET* **9**(9), 1155–1161.

[28] Qun, Z., Hua, G., Ying, G. & Youqing, B. (2006) Separation of micro-Doppler signal using an extended Hough transform, *in International Conference on Communications, Circuits and Systems Proceedings*, pp. 361–365.

[29] Zhang, Q., Yeo, T. S., Tan, H. S. & Luo, Y. (2008) Imaging of a moving target with rotating parts based on the Hough transform, *IEEE Transactions On Geoscience and Remote Sensing* **46**(1), 291–299.

[30] Luo, Y., Zhang, Q., Qiu, C.-W., Liang, X.-J. & Li, K.-M. (2010) Micro-Doppler effect analysis and feature extraction in ISAR imaging with stepped-frequency chirp signals, *IEEE Transactions on Geoscience and Remote Sensing* **48**(4), 2087–2098.

[31] Thayaparan, T., Abrol, S., Riseborough, E., Stankovic, L., Lamothe, D. & Duff, G. (2007) Analysis of radar micro-Doppler signatures from experimental helicopter and human data, *Radar, Sonar & Navigation, IET* **1**(4), 289–299.

[32] Yuan, B., Chen, Z. & Xu, S. (2014) Micro-Doppler analysis and separation based on complex local mean decomposition for aircraft with fast-rotating parts in ISAR imaging, *IEEE Transactions on Geoscience and Remote Sensing* **52**(2), 1285–1298.

[33] Li, K.-M., Liang, X.-J., Zhang, Q., Luo, Y. & Li, H.-J. (2011) Micro-Doppler signature extraction and ISAR imaging for target with micromotion dynamics, *IEEE Geoscience and Remote Sensing Letters* **8**(3), 411–415.

[34] Selesnick, I. W. (2011) Resonance-based signal decomposition: A new sparsity-enabled signal analysis method, *Signal Processing* **91**(12), 2793 – 2809.

[35] Sweldens, W. (1995) Lifting scheme: a new philosophy in biorthogonal wavelet constructions, *in SPIE's 1995 International Symposium on Optical Science, Engineering, and Instrumentation*, pp. 68–79.

[36] Blu, T. (1998) A new design algorithm for two-band orthonormal rational filter banks and orthonormal rational wavelets, *IEEE Transactions on Signal Processing* **46**(6), 1494–1504.

[37] Bayram, I. & Selesnick, I. W. (2007) Design of orthonormal and overcomplete wavelet transforms based on rational sampling factors, *in Proc. Wavelet Applications in Industrial Processing*.

[38] Selesnick, I. (2011) Wavelet transform with tunable Q-factor, *IEEE Transactions on Signal Processing* **59**(8), 3560–3575.

[39] Bayram, I. & Selesnick, I. (2009) Frequency-domain design of overcomplete rational-dilation wavelet transforms, *IEEE Transactions on Signal Processing* **57**(8), 2957 –2972.

[40] Nguyen, S. T. N. & Ng, B. W.-H. (2013) Bi-orthogonal rational discrete wavelet transform with multiple regularity orders and application experiments, *Signal Processing* **93**(11), 3014–3026.

[41] Nguyen, N. S. T. (2014) *Design of bi-orthogonal rational discrete wavelet transform and the associated applications*, PhD thesis, University of Adelaide.

[42] Nguyen, S. & Al-Ashwal, W. (2015) Sea clutter mitigation using resonance-based signal decomposition, *IEEE Geoscience and Remote Sensing Letters* **12**(11), 2257–2261.

[43] Chen, S. S., Donoho, D. L. & Saunders, M. A. (2001) Atomic Decomposition by Basis Pursuit, *SIAM Review* **43**, 129–159.

[44] Afonso, M. V., Bioucas-Dias, J. M. & Figueiredo, M. A. (2010) Fast image recovery using variable splitting and constrained optimization, *IEEE Transactions on Image Processing* **19**(9), 2345–2356.

[45] Horst, M. M., Dyer, F. B. & Tuley, M. T. (1978) Radar sea clutter model, *in International IEEE AP/S URSI Symposium*, pp. 6–10.

[46] Melino, R., Kodituwakku, S. & Tran, H.-T. (2015) Orthogonal matching pursuit and matched filter techniques for the imaging of rotating blades, *in IEEE Radar Conference*.

DEFENCE SCIENCE AND TECHNOLOGY GROUP DOCUMENT CONTROL DATA		1. DLM/CAVEAT (OF DOCUMENT)	

| 2. TITLE

Signal Separation Of Helicopter Radar Returns Using Wavelet-Based Sparse Signal Optimisation | 3. SECURITY CLASSIFICATION (FOR UNCLASSIFIED REPORTS THAT ARE LIMITED RELEASE USE (L) NEXT TO DOCUMENT CLASSIFICATION)

Document   (U)
Title   (U)
Abstract   (U) | | |

| 4. AUTHORS

Si Tran Nguyen Nguyen, Sandun Kodituwakku, Rocco Melino and Hai-Tan Tran | 5. CORPORATE AUTHOR

Defence Science and Technology Group
PO Box 1500
Edinburgh, South Australia 5111, Australia | | |

6a. DST Group NUMBER DST-Group–RR–0436	6b. AR NUMBER 016–709	6c. TYPE OF REPORT Research Report	7. DOCUMENT DATE October, 2016

8. Objective ID	9. TASK NUMBER	10. TASK SPONSOR	

13. DST Group Publications Repository `http://dspace.dsto.defence.gov.au/dspace/`	14. RELEASE AUTHORITY Chief, National Security and ISR Division		

15. SECONDARY RELEASE STATEMENT OF THIS DOCUMENT

Approved for public release

OVERSEAS ENQUIRIES OUTSIDE STATED LIMITATIONS SHOULD BE REFERRED THROUGH DOCUMENT EXCHANGE, PO BOX 1500, EDINBURGH, SOUTH AUSTRALIA 5111

16. DELIBERATE ANNOUNCEMENT

No Limitations

17. CITATION IN OTHER DOCUMENTS

No Limitations

18. RESEARCH LIBRARY THESAURUS

Helicopter radar returns, Signal separation, Wavelet transform, Sparse signal representation

19. ABSTRACT

A novel wavelet-based sparse signal representation technique is used to separate the main and tail rotor blade components of a helicopter from the composite radar returns. The received signal consists of returns from the rotating main and tail rotor blades, the helicopter body, possible land or sea clutter, and other residual components, which may all overlap in time and frequency; and therefore conventional time and frequency separation techniques cannot be applied. A sparse signal representation technique is now proposed for this problem with the tunable Q wavelet transform used as the dictionary. The proposed algorithm is demonstrated using both simulated and real radar data (X and Ku-band), and is capable of extracting the components of interest successfully.